View metadata, citation and similar papers at core.ac.uk
brought to you by CORE
provided by NASA Technical Reports Server

ACOUSTIC ANALYSIS OF SENSOR PORTS

M. J. Casiano
NASA Marshall Space Flight Center
Huntsville, AL

ABSTRACT

Acquiring data in rocket engines that is representative of the actual dynamic environment can often be difficult due to a multitude of influences. One source of contamination that is often not considered entirely is the response associated with the acoustic cavity created by a sensor offset. It is common to offset a sensor due to various reasons such as for mounting accessibility, thermal isolation, shock reduction, or prevention of debris impingement. While estimating the natural frequency of the acoustic cavity is straightforward, limited analysis has been described on the determination of the overall frequency response. The sensor port design approach usually attempts to ensure the port is short enough such that the acoustic response is negligible near the frequency-of-interest, but this requires knowledge of the frequency response and simple rules-of-thumb are not always guaranteed. Data correction and/or data interpretation is also often desired for an unsatisfactory response. The limited response analysis in the literature only offers approximations or neglects important contributions. A new approach is devised theoretically and computationally that captures the true acoustic response of a sensor port. This paper summarizes the acoustics background, the port response theoretical development, and provides comparisons of a port acoustic response using an analytical model and computational acoustics. The effects of nonlinear acoustics are also examined. Additionally, the paper summarizes the design of a specialized filter using the predicted sensor port response that can be applied to data for correction.

INTRODUCTION

Acquiring data that is representative of an environment can often be difficult due to a multitude of influences. Unwanted responses can be caused by every component in the measurement system such as those due to the acquisition system electronics, transducer sensing components, and cables. Mains electrical noise may often taint data in a poorly grounded system. Moreover, the sensor transducer component, such as piezoelectric crystals, have a sensitivity to other environments that can also corrupt the data, such as the thermal and vibratory influence on a dynamic pressure device. Careful design of the measurement system is always prudent prior to data collection.

There is another source of contamination that is often not considered entirely, particularly for dynamic pressure sensors. It may not always be possible to install a dynamic pressure sensor so that it is mounted flush with the environment of interest. In addition, it is common to offset the sensor due to various reasons such as for mounting accessibility, thermal isolation, shock reduction, or prevention of debris impingement. This offset, or standoff, creates an acoustic cavity with the sensing device in the back of the cavity. The acoustic cavity is referred to as a sensor port. The sensor port is part of the system being measured, but it is not part of the system that is intended to be measured. While the sensor port may be small, its contribution to the collected data may be very significant. Figure 1 shows generic sensor mounting schemes in the desired configuration and in an offset configuration that produces a sensor port.

While estimating the natural frequency of the acoustic cavity is straightforward, limited analysis has been described on the determination of the overall frequency response. The acoustic resonance within the sensor port produces a frequency-dependent amplification and phase deviation that directly affects the data collected. The desired port configuration is usually flush mounted, but acceptable

Statement A: Approved for public release; distribution is unlimited.

configurations can be close coupled such that frequencies-of-interest are negligibly affected by the influence of the port.

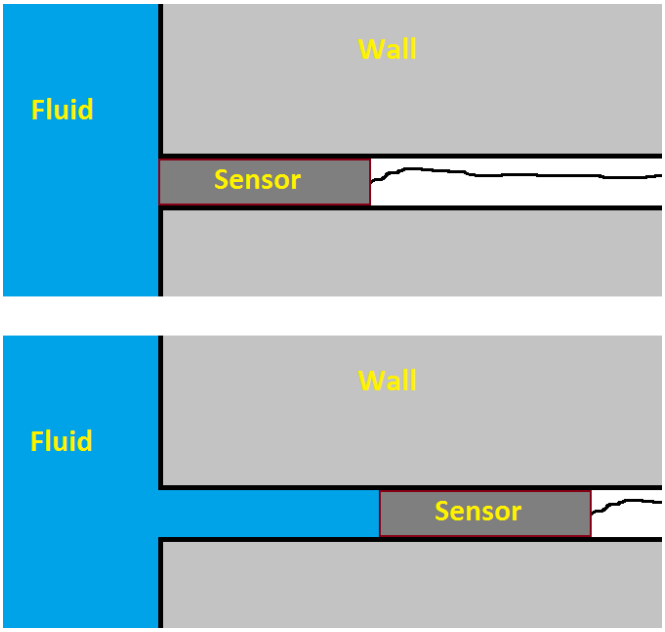

Figure 1. Desired Configuration (top) and Offset Configuration with Sensor Port (bottom)

The sensor port design approach usually attempts to ensure the port is short enough such that the acoustic response is negligible near the frequency-of-interest, but this requires knowledge of the frequency response and simple rules-of-thumb are not always guaranteed. The design estimate using simple calculations may also be very conservative, for example where a longer port may be adequate in a configuration with a mounting limitation. Furthermore, it is often desired to understand the frequency response in situations where an undesirable sensor port exists for data correction and/or data interpretation.

The purpose of this paper is to provide background, relevant theory, and examples for acoustic response analysis of a sensor port. The goal is to be able to predict the sensor port response and understand what effect the port has on the collected data.

RESULTS AND DISCUSSION

ANALYTICAL MODELING

The primary purpose of analytical modeling is to obtain an accurate solution in an efficient manner. An analytical framework allows for development of tractable solutions that can be applied quickly. It is very important to understand the constraints and assumptions that are used in the development of an analytical model so that the model is not used outside of the intended scope.

Sensor Port Design Guideline

A sensor port can be approximated as a cylindrical acoustic waveguide with a single effective diameter and a total length. The wave equation can be solved in this domain with appropriate boundary conditions. For a cylindrical cavity, the natural frequency and shape of the mode can then be predicted. The longitudinal modes are the relevant modes that produce amplification on the pressure sensor diaphragm. The fundamental longitudinal mode shape is that of a quarter wave and the natural frequency

is given as eq. (1), where $\overline{c}$ is the sound speed, L is the total length, and f_n is the natural frequency.[1] p. 343

$$f_n = \frac{\overline{c}}{4L} \tag{1}$$

A correction is made because the open boundary condition is not truly a pressure release boundary. A general impedance exists at this boundary due to the local pressure radiating from the end into the fluid outside the port. An end correction for a flanged tube can be derived where a flanged tube represents a tube that opens through a plane baffle of infinite extent. Equation (2), a low frequency estimate, can be derived by considering first order terms where R is the radius at the opening and ΔL is an end correction.[2] pp. 151-152, [3] pp. 272-274

$$\Delta L \approx \frac{8R}{3\pi} \tag{2}$$

The quarter wave natural frequency of a flanged sensor port can then be estimated using eq. (3) where the effective length is given by $L' = L + \Delta L$. This is the traditional form used in identifying the fundamental resonance frequency of a flanged quarter-wave resonator.

$$f_n = \frac{\overline{c}}{4L'} \tag{3}$$

Given the quarter wave natural frequency, rules-of-thumb vary for predicting an acceptable bandwidth. Criteria for many applications range between 3x to 5x lower than the natural frequency and are based on the amount of gain response (or pressure amplification) that is acceptable, for example a 3x factor is recommended in references [**4** p. 464, **5** p. 63] for combustion stability. The ratio, $M = f_n / f_i$, used commonly as criteria for sensor port design, can be referred to as the frequency multiplication factor. It is described as the ratio of the natural frequency to the maximum frequency-of-interest, f_i. To generate estimates for the gain and error associated with a particular frequency multiplication factor, the acoustics in the sensor port can be surmised to follow a forced time-harmonic oscillator response of a single-degree-of-freedom system (SDOF).

The pressure gain associated with the sensor port can be roughly estimated by considering an undamped SDOF solution. This approximation provides a reasonable estimate, however the undamped SDOF response may not necessarily produce the worst-case amplification over the entire frequency bandwidth. The gain for an undamped SDOF, D, given in eq. (4), provides the magnification at the maximum frequency of interest. It can also be written in terms of the frequency multiplication factor where values close to 1 are obviously not applicable as the gain approaches infinity for an undamped system.

$$D = \frac{1}{1-\left(f_i / f_n\right)^2} = \frac{M^2}{M^2 - 1} \tag{4}$$

This undamped gain is classically used as a guide to represent the upper bound of the pressure amplification factor. However, the acceptable range defining a flat useable bandwidth is ultimately determined by the analyst or end user. To aid with this definition, the relative error, ε, associated with the undamped response gain can be calculated considering that the ideal exact gain for a flush-mounted sensor is equal to a value of 1 (no amplification).

$$\varepsilon = \left| \frac{D_{exact} - D_{est.}}{D_{exact}} \right| = \left| 1 - D_{est.} \right| \tag{5}$$

Using eq. (4) for the gain estimate, the gain error in eq. (5) is given simply as eq. (6).

$$\varepsilon = D - 1 = \frac{1}{M^2 - 1} \tag{6}$$

For the example rule-of-thumb described earlier, the error can simply be calculated considering that the system behaves as an undamped SDOF. Equation (6) can be used to show that for $M = 3$ the error is 12.5% and for $M = 5$ the error is 4.2%. As another example, it is often established that the gain error is within a certain percentage. In the example where a flat useable bandwidth is specified to be within 5%, the frequency multiplication factor can be calculated to be $M = 4.6$; therefore, the maximum frequency-of-interest must be approximately 4.6x lower than the natural frequency for the response to be within this error.

These examples can be used as design guidance, and in some cases, the port length may need to be shortened so that this criterion is met. Using eq. (3), and the multiplication factor, a design length, L_i, is derived in eq. (7). The inequality denotes that smaller lengths are acceptable.

$$L_i \leq \frac{\bar{c}}{4 f_i M} - \frac{8R}{3\pi} \tag{7}$$

The design length can also be described in a more useful form by incorporating a specified flat useable bandwidth. This specification would include the gain relative error and maximum frequency-of-interest. Substituting eq. (6) into eq. (7) produces this practical formula as eq. (8).

$$L_i \leq \sqrt{\frac{\varepsilon}{\varepsilon + 1}} \cdot \frac{\bar{c}}{4 f_i} - \frac{8R}{3\pi} \tag{8}$$

While these relationships provide a guide for a sensor port design, they do not produce a representative frequency response. The simple design guide may also break down in many cases, e.g., the undamped SDOF model may not apply over the bandwidth-of-interest or the guide may be inaccurate for a complex multi-port design. Also, the port design may not be practical to construct, and a more accurate estimate may provide a viable standoff length. Additionally, accurate estimates for correcting data with port resonances at various frequencies may also be desired.

Sensor Port Frequency Response Model - Theory

The goal is to be able to predict an accurate sensor port response by modeling the port acoustic cavity frequency response. As an improvement to the undamped SDOF model used classically, a theory is developed for obtaining the acoustic frequency response of a sensor port. There are three critical advancements necessary to extend classic acoustic theory into a practical sensor port frequency response model: 1) application of the distributed acoustic models rather than the lumped acoustic element approach, which relies on the long wavelength limit, 2) development of an exact solution to the thermoviscous wave equation applicable to the framework, and 3) reformulation of acoustic radiation impedance as an acoustic propagation constant. The entire development is discussed along with these theoretical improvements in the following sections.

To obtain the frequency response, the complex pressure ratio is explored. This pressure transfer function or complex pressure ratio is an important quantity, which measures the complex pressure of the output to the input.

$$H = \frac{\hat{p}_{out}}{\hat{p}_{in}} \tag{9}$$

In the frequency domain, two important parameters provide information about the response. These are the pressure amplification factor, X, and relative phase, ϕ. Both these parameters can be obtained from the complex pressure ratio and are functions of frequency.

A pressure amplification factor is also referred to as an amplification factor or gain. The pressure amplification factor[2 p. 155, 3 p. 285] of a resonator is the ratio of the acoustic pressure amplitude at the back of the sensor port, i.e., the measurement location, to the acoustic pressure amplitude of an incident wave on the sensor port. i.e., without influence of the port. The relative phase is simply the deviation in phase angle between the pressure at the back of the sensor port and the incident pressure wave on the sensor port. For both analytical and numerical modeling, the influence of the port must be appropriately handled as not to obscure the incident pressure field.

In the following theory, the output is the upstream end defined at the sensor port back (at the measurement location). In a 1-D sense, the input of the sensor port is represented somewhat abstractly as the location downstream of the end correction region. The effects of the end correction region can be captured appropriately by incorporating the physical influences using a transfer line model with an independent line segment; these radiation effects will be discussed in detail later. The transfer line model will be discussed as the acoustic framework in this section.

Using subscript U for the upstream boundary and subscript D for the downstream boundary, the modulus and argument of the complex pressure ratio are written as eq. (10) and eq. (11). These are referred to as the pressure amplification factor and relative phase, respectively. The upstream and downstream transfer line nomenclature are adopted from reference [**6**]. These equations together will be referred to as the sensor port response.

$$X(f) = \left| \frac{\hat{p}_U}{\hat{p}_D} \right| \tag{10}$$

$$\phi(f) = \angle \left(\frac{\hat{p}_U}{\hat{p}_D} \right) \tag{11}$$

There are many different forms of dissipation that may apply to an acoustic system. Examples include dissipation due to thermal heat conduction and viscous absorption in a fluid, thermal heat conduction and viscous absorption at a boundary, molecular relaxation, and other flow or acoustic induced dissipation mechanisms. The physical process of each mechanism is different and therefore the governing equations differ. However, while each mechanism is described by a separate lossy wave equation, their solution form remains identical. Considering that a time-harmonic signal, eq. (12), represents the wave equation pressure solution.[2 pp. 46] It is described in terms of either complex wavenumber or propagation constant, which characterize the propagation losses of an individual mechanism.[2 pp. 299, 302, 3 p. 212, 6 p. 291, 7 p. 4] Note the hat notation shown previously is dropped for the complex pressure in the remaining part of the paper. Also note that in the paper, k without the hat is the wavenumber, $k = \omega/\overline{c}$, and γ without the hat is the specific heat ratio.

$$p' = \overline{P} e^{i\omega t} e^{-i\hat{k}x} = \overline{P} e^{i\omega t} e^{-\hat{\gamma}x} \tag{12}$$

The relationship between propagation constant and complex wavenumber is given by $\hat{\gamma} = i\hat{k}$. The complex wave number and complex propagation constant for an outgoing wave moving in the positive direction is given as eq. (13) and eq. (14), respectively, shown with a real and imaginary part.[2 p. 299, 3 p. 212, 6 p. 291, 7 p. 4] The complex propagation constant is preferred in the following framework, however, the complex wave number is convenient in some cases.

$$\hat{k}_+ = \beta - i\alpha \tag{13}$$

$$\hat{\gamma}_+ = \alpha + i\beta \tag{14}$$

The incoming wave is given by the negative of eq. (13) and eq. (14), however for discussion the outgoing wave is examined. Equation (12) can then be written as an outgoing pressure wave, expanded as eq. (15).[2] p. 302, [3] p. 212, [6] p. 291

$$p' = \bar{P}_+ e^{i\omega t} e^{-(\alpha + i\beta)x} = \bar{P}_+ e^{i\omega t} e^{-\alpha x} e^{-i\beta x} \tag{15}$$

The spatial absorption coefficient is α, and is seen by inspection of eq. (15) since the amplitude decays spatially by $e^{-\alpha x}$. The parameter β is a phase shift parameter (confusingly it is sometimes referred to as the propagation constant) and is related to the phase speed, c_p, by eq. (16).

$$c_p = \frac{\omega}{\beta} \tag{16}$$

The solution to the lossy wave equations given by eq. (12) or expanded as eq. (15) show that the pressure represents an attenuating pressure oscillation with the wave propagation speed given by the phase speed. Because the solution to lossy wave equations describing different physical processes can all be represented using the same functional form, it is possible to describe a propagation constant that is specific for each physical mechanism. Therefore, the phase speed and spatial absorption coefficient can also be described for any particular lossy wave equation associated with a specific dissipation mechanism.

The Helmholtz equation represents the time-independent form of the wave equation and can be used as a consistent theoretical framework that satisfies the solution form of eq. (15). This framework is useful to obtain sensor port relationships. It is also useful to represent the solution in terms of impedance, which is a function of frequency, since the desire is to obtain the frequency response. The specific acoustic impedance is given as eq. (17).

$$Z = \frac{p'}{u'} \tag{17}$$

A 'pipe' section is used to develop a formulation that can be applied to a sensor port. This is schematically shown in Figure 2. The characteristic impedance, Z_C, and propagation constant are dependent on the pipe section geometry and fluid properties. The mean velocity arrow indicates the direction of flow and resulting upstream and downstream nomenclature.

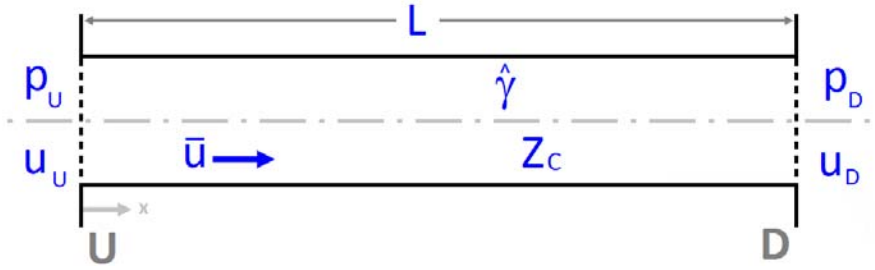

Figure 2. Pipe-section Schematic

The equations of motion are described using the momentum equations, continuity equation, and equation of state.[2] pp. 27-39, 299 [6] pp. 289-293 By linearizing and applying a separation-of variables-technique, the governing equations can be split into a spatially dependent and temporally dependent form.[6] p. 291 The spatially dependent form is the Helmholtz equation and will be examined carefully here. Applying the upstream boundary conditions to the pipe section gives the solution as a function of axial position and can be described as eq. (18) and eq. (19).[6] pp. 289-293 These distributed solutions are referred to as transfer equations and are the basis for distributed element models. Applying this distributed element model to a

sensor port is necessary to correctly predict the acoustic frequency response, since the classic lumped acoustic element approach only applies in the long wavelength limit.[3 p. 283]

$$\breve{p}(x) = p_U \cosh(\hat{\gamma}x) - Z_C u_U \sinh(\hat{\gamma}x) \tag{18}$$

$$\breve{u}(x) = -\frac{p_U}{Z_C}\sinh(\hat{\gamma}x) + u_U \cosh(\hat{\gamma}x) \tag{19}$$

Typically, these may be seen in literature written in terms of exponential functions, however hyperbolic trigonometric functions simplify the solution form and provide a means of convenient manipulation. The characteristic impedance of the fluid for an outgoing wave, written in terms of the propagation constant, can be determined by calculating the ratio given in eq. (20) for an outgoing wave.[2 pp. 38-39, 3 p. 126, 6 pp. 291-292] The relationship can be derived by examining the only the outgoing wave using the ratio of pressure, eq. (12), to the analogous form for velocity.

$$Z_C \equiv \left(\frac{p'}{u'}\right)_+ = -\frac{\overline{\rho}\,\overline{c}^2\hat{\gamma}}{\omega g_c} i \tag{20}$$

One particular pair of transfer equations is very useful in manipulating sensor port relationships. By substituting $x = L$ into eq. (18) and eq. (19), where $p(L) = p_D$ and $u(L) = u_D$, and solving for the upstream conditions, the following relationships are obtained.

$$p_U = p_D \cosh(\hat{\gamma}L) + Z_C u_D \sinh(\hat{\gamma}L) \tag{21}$$

$$u_U = \frac{p_D}{Z_C}\sinh(\hat{\gamma}L) + u_D \cosh(\hat{\gamma}L) \tag{22}$$

Using eq. (21) and eq. (22), the downstream impedance can be written in terms of the upstream impedance.

$$Z_D = \frac{Z_U - Z_C \tanh(\hat{\gamma}L)}{1 - \frac{Z_U}{Z_C}\tanh(\hat{\gamma}L)} \tag{23}$$

The distributed solutions and relationships given in this section are used as a general acoustic framework to describe the propagation of waves within a sensor port. The propagation constants that are used in the sensor port model will be detailed following the line model discussion.

Sensor Port Frequency Response Model – 1-line model

This section develops the analytical expressions for a 1-line model using the schematic shown in Figure 3.[8] The 1-line sensor port model is most applicable to very long sensor ports with a constant diameter, where the end correction is negligible. It is applicable in modeling thermoviscous effects and is not general enough to account for radiation acoustics. Notice the upstream end is a closed boundary; this would represent the location of the sensor diaphragm. For any sensor port analysis, it is recommended that at least a 2-line model is applied so that both thermoviscous effects and radiation acoustics can be incorporated. In the 1-line model, the propagation constant is a function of the thermoviscous spatial absorption coefficient. This model is primarily included for completeness, since radiation effects cannot be incorporated into the model. Also note that since in general there will be multiple-line models making up a complex sensor port, a numbering scheme is used instead of the upstream and downstream notation.

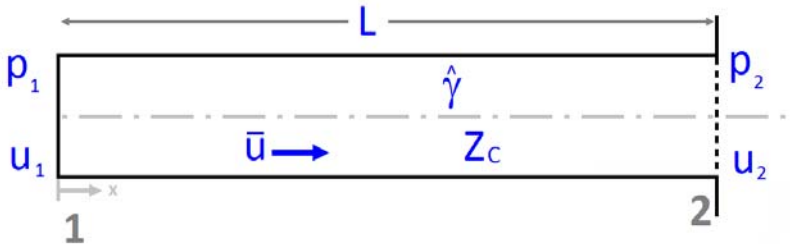

Figure 3. Pipe-section Schematic for 1-Line Sensor Port

The complex pressure ratio of a 1-line port can be derived simply. Using eq. (21) as a general line segment relationship, the formula for a complex pressure ratio of a pipe section is obtained by dividing by the downstream pressure, p_2, shown as eq. (24).

$$\frac{p_1}{p_2} = \cosh(\hat{\gamma}L) + \frac{Z_C}{Z_2}\sinh(\hat{\gamma}L) \tag{24}$$

For a closed boundary, the location 1 impedance is infinite. By applying this limit to eq. (23), the location 2 boundary impedance simplifies to eq. (25).

$$\lim_{Z_1 \to \infty} Z_2 = -Z_C \cdot \coth(\hat{\gamma}L) \tag{25}$$

Substituting eq. (25) into eq. (24) results in the complex pressure ratio for a 1-line port and simplifies to eq. (26).

$$\frac{p_1}{p_2} = \operatorname{sech}(\hat{\gamma}L) \tag{26}$$

Using eq. (10) and eq. (11), the pressure amplification factor and relative phase are found as eq. (27) and eq. (28), respectively, denoted using the real part, $\Re$, and imaginary part, $\Im$. The function $\tan 2^{-1}(y,x)$ is the 2-argument arctangent (also called the four-quadrant inverse tangent) and can also be represented mathematically as the argument function, $\arg(x+iy)$.

$$X(f) = \left|\operatorname{sech}(\hat{\gamma}L)\right| = \sqrt{\Im\left(\operatorname{sech}(\hat{\gamma}L)\right)^2 + \Re\left(\operatorname{sech}(\hat{\gamma}L)\right)^2} \tag{27}$$

$$\phi(f) = \angle\left(\operatorname{sech}(\hat{\gamma}L)\right) = \tan 2^{-1}\left(\Im\left(\operatorname{sech}(\hat{\gamma}L)\right), \Re\left(\operatorname{sech}(\hat{\gamma}L)\right)\right) \tag{28}$$

For a 1-line model, the pressure amplification and relative phase can be described by plotting these equations as a function of frequency.

Sensor Port Frequency Response Model – 2-line model

This section develops the analytical expressions for a 2-line model. The 2-line sensor port model is general enough to consider damping effects due to thermoviscous acoustics and acoustic radiation out of the port, for a constant diameter port. In this model, a propagation constant would be defined for thermoviscous effects and another propagation constant for acoustic radiation. A schematic drawing with two equal-diameter segments is shown in Figure 4, now with a midstream location separating the line segments. Line segment A will represent the actual port length and thermoviscous effects and line segment B will represent the end correction for acoustic radiation.

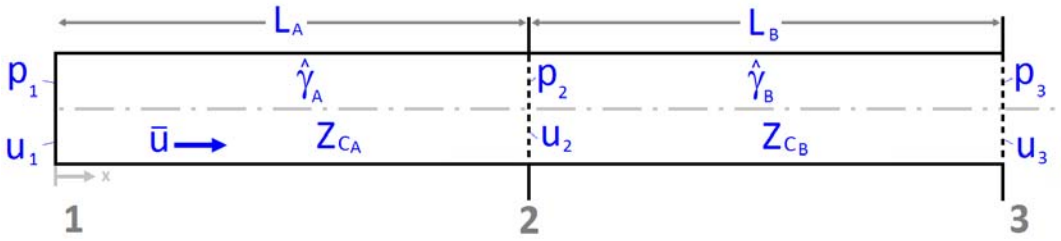

Figure 4. Pipe-section Schematic for 2-Line Sensor Port

The 2-line model expressions can be derived by first examining just pipe section A using eq. (21), but dividing through by the far downstream pressure, p_3. This results in eq. (29).

$$\frac{p_1}{p_3} = \frac{p_2}{p_3}\cosh(\hat{\gamma}_A L_A) + \frac{u_2}{p_3} Z_{C,A} \sinh(\hat{\gamma}_A L_A) \tag{29}$$

Now expressions are only needed for p_2/p_3 and for u_2/p_3. The former can be found simply by examining pipe section B using eq. (21) and dividing through by p_3. This results in eq. (30).

$$\frac{p_2}{p_3} = \cosh(\hat{\gamma}_B L_B) + \frac{Z_{C,B}}{Z_3}\sinh(\hat{\gamma}_B L_B) \tag{30}$$

The latter can be found simply by also examining pipe section B using eq. (22) and dividing through by p_3. This results in eq. (31).

$$\frac{u_2}{p_3} = \frac{1}{Z_{C,B}}\sinh(\hat{\gamma}_B L_B) + \frac{1}{Z_3}\cosh(\hat{\gamma}_B L_B) \tag{31}$$

The impedance at location 3 in eq. (30) and eq. (31) is the only remaining unknown variable. This can be found from the boundary condition at location 1. Pipe section A is examined using eq. (23) and the closed boundary impedance limit is applied, $Z_1 \to \infty$. This results in eq. (32) at location 2.

$$\lim_{Z_1 \to \infty} Z_2 = -Z_{C,A} \cdot \coth(\hat{\gamma}_A L_A) \tag{32}$$

Subsequently, pipe section B can be examined also using eq. (23) with the substitution of eq. (32) for Z_2. This results in a cumbersome impedance relationship at location 3, however there are no longer any remaining unknown variables.

$$Z_3 = \frac{-\dfrac{Z_{C,A}}{\tanh(\hat{\gamma}_A L_A)} - Z_{C,B}\tanh(\hat{\gamma}_B L_B)}{1 + \dfrac{Z_{C,A}}{Z_{C,B}}\dfrac{\tanh(\hat{\gamma}_B L_B)}{\tanh(\hat{\gamma}_A L_A)}} \tag{33}$$

Equation (30), eq. (31), and eq. (33) can now be substituted into eq. (29). After a fair amount of manipulation and simplification, a relationship can be found for p_1/p_3. Equation (34) is the complex pressure ratio for a 2-line model.

$$\frac{p_1}{p_3} = \left(\cosh(\hat{\gamma}_A L_A)\cosh(\hat{\gamma}_B L_B) + \frac{Z_{C,B}}{Z_{C,A}}\sinh(\hat{\gamma}_A L_A)\sinh(\hat{\gamma}_B L_B) \right)^{-1} \tag{34}$$

For a 2-line model, the pressure amplification factor and relative phase can be described by applying eq. (10) and eq. (11) to eq. (34). This formula is an important relationship and it should be emphasized that it is the simplest form possible needed to represent both thermoviscous effects and radiation acoustics for a constant diameter sensor port, both of which are necessary to produce an accurate sensor port acoustic response.

Sensor Port Frequency Response Model – Multiple-line model

For a sensor port with several segments, a multiple line model can be used to obtain the complex pressure ratio. However, it becomes simpler to solve the formulation numerically. A transfer matrix approach can also be adapted to ports of many sections.[6 p. 295, 9] However, the development described in the previous section can easily be extended recursively to any number of line segments. A pseudocode is given below as an example. In this manner, it can be extended to consider damping effects due to thermoviscous acoustics, dissipation due to acoustic radiation out of the port, and a port with multiple diameter changes.

The pseudocode provides an outline to obtain the complex pressure ratio from the aft end of a sensor port to the inlet end. The numbering scheme in the Figure 5 multi-line schematic is used for the code numerical indexing. Note that the pseudocode below is written considering an infinite impedance at the back end. However, a simple modification can be made to incorporate a general diaphragm or wall impedance by defining the value of the location 1 impedance, removing the line describing the location 2 impedance, and modifying the impedance calculation loop to begin at index 2.

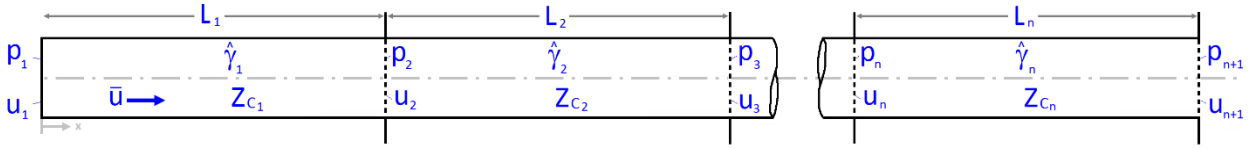

Figure 5. Pipe-section Schematic for Programming Logic in Multi-Line Sensor Port

Pseudocode to obtain sensor port complex transfer equation

```
Input: n // number of line segments
Input: γk // propagation constant for each line segment
Input: Zc,k // characteristic impedance for each line segment
Input: Lk // length of each line segment

// use this formula if there is a 1-line segment, otherwise skip ahead
if n=1 then
        pp1 = sech(γ1 · L1)
        end
end if

// obtain impedance at inlet, Zn+1, based on aft end impedance condition, Z1
Z1 = inf
Z2 = -Zc,1 / tanh(γ1 · L1)
for k = 3 to n+1 by +1 do
        Zk = [Zk-1 - Zc,k-1 · tanh(γk-1 · Lk-1)]/[1 - Zk-1 / Zc,k-1 · tanh(γk-1 · Lk-1)]
end for

// obtain transfer equation p1/pn+1 using uk/pn+1 and pk/pn+1
upn = 1 / Zc,n · sinh(γn · Ln) + 1 / Zn+1 · cosh(γn · Ln)
ppn = cosh(γn · Ln) + Zc,n / Zn+1 · sinh(γn · Ln)
for k = n-1 to 1 by -1 do
        upk = ppk+1 / Zc,k · sinh(γk · Lk) + upk+1 · cosh(γk · Lk)
        ppk = ppk+1 · cosh(γk · Lk) + upk+1 · sinh(γk · Lk)
end for

// display transfer equation p1/pn+1
disp pp1

end
```

As done previously, the last line segment should include parameters associated with acoustic radiation. Also note that several input variables are additionally functions of frequency and would need to be evaluated over the entire frequency range, i.e., propagation constant, characteristic impedance, and length (specifically the radiation end correction length).

Thermoviscous Boundary Dissipation

The acoustic framework is described previously; however, the propagation constants remain undetermined. The propagation constant contains information about the decay rate and phase speed of the propagating wave. This section gives background on thermoviscous boundary dissipation, and the following two sections provide a thermoviscous propagation constant. Following the sections on thermoviscous effects, radiation acoustics and an associated propagation constant will be discussed, which can be used in the frequency response models.

Acoustic dissipation in a fluid is considered by studying the propagation of acoustic waves with thermal and viscous losses. Reference [**8**] provides a summary of these thermoviscous effects including description of absorption coefficients for several different thermoviscous mechanisms. Sources of thermoviscous dissipation can be broken into two categories: damping mechanisms intrinsic to the medium and those associated with the boundary.[**3** p. 210]

The damping mechanisms intrinsic to the medium are generally very small and are often applicable to dissipation over long distances. Example intrinsic mechanisms include viscous dissipation due to relative particle motion between the compressions and expansions of a sound wave, heat conduction from a higher temperature condensation to a lower temperature rarefaction, or various molecular processes. This mode of absorption is negligible on the scale of sensor ports and not considered here.

The damping mechanisms associated with the boundary are discussed in references [**2** pp. 322-324, 519-525] and [**3** pp. 228-234] and are important for sensor port analysis. Boundary dissipation occurs due to the passage of a wave over a surface boundary. At a wall, there are viscous losses due to an acoustic shear layer and thermal losses due to heat transfer between the adiabatic fluid and isothermal wall. Both viscous and thermal effects result in the loss of energy from the propagating wave. This mode of damping is relevant in areas with small dimensions, such as in sensor ports, where an acoustic thermal and viscous boundary layer exist. Similar to a boundary layer that is caused by a steady flow, acoustic waves generate an acoustic boundary layer. The acoustic boundary layer is much thinner because the oscillatory flow continually changes direction limiting the boundary layer growth.

In general, thermoviscous acoustics problems can be solved directly using continuity, Navier-Stokes, and an energy equation along with appropriate constitutive equations (Stokes expression, Fourier heat conduction law, and equation of state). Rather than examining the complete set of equations, which would need to be solved numerically, a simpler description is useful in determining the thickness of the acoustic boundary layers. The boundary layer thickness for the oscillating flow is defined as the distance over which the shear-wave amplitude decays to $1/e$.

By independently examining the effect of viscosity on oscillatory wave motion, an acoustic viscous boundary layer thickness can be derived, and is given as eq. (35).[**2** pp. 520-523]

$$\delta_{\mu} = \sqrt{\frac{2\mu}{\omega\bar{\rho}}} \tag{35}$$

Similarly, by examining the effect of a thermal conduction on oscillatory wave motion, the acoustic thermal boundary layer thickness can be written as eq. (36).[**3** p. 232]

$$\delta_\kappa = \sqrt{\frac{2\mu}{\omega\bar{\rho}\,\mathrm{Pr}}} \tag{36}$$

The viscous boundary-layer absorption occurs because of the presence of viscosity in the fluid. Fluid particles oscillate in the main flow field, but fluid particles adjacent to the wall adhere to the wall. A transition where the oscillation amplitude decreases from the nominal amplitude in the main flow field down to zero at the wall occurs.[2 p. 322]

The thermal boundary-layer absorption occurs because acoustic oscillations in the main flow field occur adiabatically, however near the pipe wall the oscillatory flow is isothermal because the wall behaves effectively as an infinite source/sink since thermal conduction in a solid is typically orders of magnitude greater than in a fluid. The particles adjacent to the wall are therefore at a constant temperature and any temperature change in adjacent fluid is immediately quenched by heat flow into or out of the wall.[2 p. 323]

A quasi-one-dimensional acoustic boundary layer model has been described in the literature where the losses associated with both the viscous and thermal boundary layer are homogenized and distributed evenly across the fluid.[2 pp. 524-525, 3 pp. 230-233] The development allows simplification of the complete set of governing equations to a wave equation. Thermoviscous boundary dissipation can then be described as an effective solution and used to obtain a propagation constant.[2 pp. 324, 524] It should be noted that the domain of interest for boundary dissipation is over the length of the port geometry and not exterior of the opening. Additionally, the inequality $\delta \ll R$ must hold for this acoustic absorption model, so that the curvature of the pipe wall is much greater than either of the acoustic boundary layer thicknesses. Because of this inequality, the acoustic absorption model is sometimes referred to as the wide-pipe model. The boundary layer absorption complex wave number for this model, combining both viscous and thermal contributions, is developed in the literature as eq. (37).[2 p. 325] Note that the variable, γ, is used for specific heat ratio and not propagation constant.

$$\hat{k}_{BL} = \frac{\omega/\bar{c}}{\sqrt{1-\frac{2}{R}\sqrt{\frac{\mu}{i\omega\bar{\rho}}}\left(1+\frac{\gamma-1}{\sqrt{\mathrm{Pr}}}\right)}} \tag{37}$$

The next two sections provide two separate thermoviscous propagation constants for use in the sensor port theoretical framework. The first propagation constant is based on traditional dissipation parameters, which are derived using first order approximations of the exact complex wave number, eq. (37); a common procedure described in literature.[2 p. 325] The second propagation constant is also derived using the exact complex wave number, eq. (37), however the exact form is retained. This paper describes the procedure to reformulate the exact complex wave number into the expanded form described by eq. (14), for incorporation into the sensor port framework.

Thermoviscous Boundary Dissipation – Traditional Model

The total acoustic dissipation can be described using spatial absorption coefficients. In a region where multiple forms of thermoviscous absorption apply, the total absorption coefficient can be regarded as the sum of the absorption coefficients for the individual thermoviscous loss mechanisms, as shown in eq. (38).[3 pp. 217, 229, 233-234] Superposition is typically justified in practice, and true when losses are small, however in general they do have interactions with each other.

$$\alpha = \sum_i \alpha_i = \alpha_\mu + \alpha_\kappa + \ldots \tag{38}$$

The spatial absorption coefficient associated with viscous boundary-layer absorption and thermal boundary-layer absorption can be combined using eq. (38) into a combined boundary-layer absorption coefficient. The traditional form is presented here as eq. (39).

$$\alpha_{\mu\kappa} = \frac{1}{\bar{c}R} \cdot \sqrt{\frac{\mu\omega}{2\bar{\rho}}} \left(1 + \frac{\gamma - 1}{\sqrt{\mathrm{Pr}}} \right) \tag{39}$$

The traditional absorption coefficient for thermoviscous boundary dissipation is based on the first order approximation of eq. (37).[2 p. 325] It is also possible to show that the traditional form of phase speed can be combined and written as eq. (40).

$$c_{p,\mu\kappa} = \bar{c} \left(1 - \frac{\bar{c}}{\omega} \alpha_{\mu\kappa} \right) \tag{40}$$

The phase speed can be expanded as eq. (41).

$$c_{p,\mu\kappa} = \bar{c} - \frac{\bar{c}}{R} \sqrt{\frac{\mu}{2\omega\bar{\rho}}} \left(1 + \frac{\gamma - 1}{\sqrt{\mathrm{Pr}}} \right) \tag{41}$$

The traditional propagation constant can be reconstructed by combining eq. (39) and eq. (41) using eq. (14) and eq. (16). This is shown as eq. (42).

$$\gamma_{\mu\kappa} = \frac{1}{\bar{c}R} \cdot \sqrt{\frac{\mu\omega}{2\bar{\rho}}} \left(1 + \frac{\gamma - 1}{\sqrt{\mathrm{Pr}}} \right) + i \cdot \frac{\omega}{\bar{c}} \cdot \left(1 - \frac{1}{R} \sqrt{\frac{\mu}{2\omega\bar{\rho}}} \left(1 + \frac{\gamma - 1}{\sqrt{\mathrm{Pr}}} \right) \right)^{-1} \tag{42}$$

Thermoviscous Boundary Dissipation – Exact Model

The complex propagation constant shown in eq. (42) is the result of combining first order terms of a series expansion. This level of accuracy is traditionally used in most applications. However, improved accuracy can be achieved by using the exact complex wave number from the acoustic boundary-layer model. For conciseness, the exact complex wave number, eq. (37), is first written in terms of the traditional boundary-layer absorption coefficient as eq. (43).

$$\hat{k}_{BL} = \frac{\omega / \bar{c}}{\sqrt{\left(1 - \frac{2\bar{c}}{\omega} \alpha_{\mu\kappa} \right) + i \cdot \frac{2\bar{c}}{\omega} \alpha_{\mu\kappa}}} \tag{43}$$

An analytic expression for the propagation constant can be obtained in an exact manner by first splitting the complex wave number, eq. (43), into the real and imaginary part. The complication arises because of the difficulty in obtaining the real and imaginary part of a square root term. This can be addressed by recognizing that the principal square root is defined as eq. (44).

$$\sqrt{z} = e^{\frac{1}{2}\ln(z)} = e^{\frac{1}{2}\ln(|z|) + i\frac{1}{2}\arg(z)} \tag{44}$$

The real and imaginary parts of the square root function in the denominator of (43) can be found by first simplifying eq. (44) as eq. (45) and eq. (46), respectively.

$$\Re\left(\sqrt{z}\right) = \sqrt{|z|} \cos\left(\frac{\arg(z)}{2} \right) \tag{45}$$

$$\Im\left(\sqrt{z}\right) = \sqrt{|z|} \sin\left(\frac{\arg(z)}{2} \right) \tag{46}$$

After defining z as the radicand in the denominator of eq. (43) and also by replacing the argument function with the 2-argument arctangent function, the real and imaginary parts can then be written as eq. (47) and eq. (48). Note that the radical represents the 4th root of its radicand.

$$R_{den} = \Re\left(\sqrt{z}\right) = \sqrt[4]{\left(\left(1-\frac{2\overline{c}}{\omega}\alpha_{\mu\kappa}\right)^2 + \left(\frac{2\overline{c}}{\omega}\alpha_{\mu\kappa}\right)^2\right)} \cdot \cos\left(\frac{1}{2}\tan 2^{-1}\left(\frac{2\overline{c}}{\omega}\alpha_{\mu\kappa}, 1-\frac{2\overline{c}}{\omega}\alpha_{\mu\kappa}\right)\right) \quad (47)$$

$$I_{den} = \Im\left(\sqrt{z}\right) = \sqrt[4]{\left(\left(1-\frac{2\overline{c}}{\omega}\alpha_{\mu\kappa}\right)^2 + \left(\frac{2\overline{c}}{\omega}\alpha_{\mu\kappa}\right)^2\right)} \cdot \sin\left(\frac{1}{2}\tan 2^{-1}\left(\frac{2\overline{c}}{\omega}\alpha_{\mu\kappa}, 1-\frac{2\overline{c}}{\omega}\alpha_{\mu\kappa}\right)\right) \quad (48)$$

Now that the real and imaginary parts of the denominator are found, eq. (43) can be written concisely as eq. (49).

$$\hat{k}_{BL} = \frac{\omega/\overline{c}}{R_{den} + i \cdot I_{den}} \quad (49)$$

The real and imaginary part of eq. (49) can now be split easily and the complex wavenumber can simply be written as eq. (50).

$$\hat{k}_{BL} = \left(\frac{\omega}{\overline{c}} \cdot \frac{R_{den}}{\left(R_{den}\right)^2 + \left(I_{den}\right)^2}\right) - i \cdot \left(\frac{\omega}{\overline{c}} \cdot \frac{I_{den}}{\left(R_{den}\right)^2 + \left(I_{den}\right)^2}\right) \quad (50)$$

Using eq. (13) and eq. (14), the complex propagation constant is given by eq. (51) where the real and imaginary parts can be described using eq. (47) and eq. (48).

$$\hat{\gamma}_{BL} = \left(\frac{\omega}{\overline{c}} \cdot \frac{I_{den}}{\left(R_{den}\right)^2 + \left(I_{den}\right)^2}\right) + i \cdot \left(\frac{\omega}{\overline{c}} \cdot \frac{R_{den}}{\left(R_{den}\right)^2 + \left(I_{den}\right)^2}\right) \quad (51)$$

This form is always recommended, as it remains exact. Likely, it has not been derived previously due to the difficulty in obtaining a tractable complex expansion, however with the aid of Maple™, a computer algebra system, this complex expansion can be easily performed.

Using eq. (14) and eq. (16), the eq. (51) propagation constant can be used to write the exact absorption coefficient and exact phase speed as eq. (52) and eq. (53), respectively.

$$\alpha_{BL} = \frac{\omega}{\overline{c}} \cdot \frac{I_{den}}{\left(R_{den}\right)^2 + \left(I_{den}\right)^2} \quad (52)$$

$$c_{p,BL} = \overline{c} \cdot \frac{\left(R_{den}\right)^2 + \left(I_{den}\right)^2}{R_{den}} \quad (53)$$

Radiation Impedance

The previous three sections describe the dissipation associated with thermoviscous effects. This section will provide background on radiation acoustics, and the following section provides a propagation constant associated with radiation acoustics that can be used in the frequency response models.

An effective damping mechanism is considered that is due to the local pressure in the sensor port radiating into the fluid outside of the sensor port. Attenuation due to the geometry is not truly a damping mechanism as no absorption takes place and no energy is lost.[2] pp. 112, 298, [3] pp. 436-437 However, an effective absorption coefficient can be described that models the effect of attenuation.

As a wave propagates through a sensor port it eventually encounters an impedance at the open end. The open end is not an ideal pressure release boundary since it radiates sound into the surrounding medium. There is a non-zero impedance and therefore a pressure node is not located at the open end.

Sound in a sensor port is not all reflected back into the port. Some sound is radiated outside of the port into the surrounding medium at the open end. The surrounding medium imposes an impedance on the propagating waves. This impedance is the radiation impedance of the acoustic wave propagated into the surrounding medium.[3 p. 184] This radiation impedance results in attenuation of the acoustics in the sensor port and an added effective length to the port.

At low frequencies, the only waves that can propagate in a sensor port are plane waves. The fluid at the open end location behaves as a piston with zero mass, radiating some sound out away from the port and reflecting some sound back into the port.[10 p. 471] The radiation impedance of the open end characterizes this effect, where the radiation resistance represents energy lost from the tube and the radiation reactance represents the reflection back into the port.[10 p. 472] To be precise, the energy is not lost, but transferred to the surrounding environment. However, in the context of the port domain, this energy transferred out of the port is modeled as an effective absorption coefficient, assuming the acoustic motion at the opening behaves as an oscillatory piston. At higher frequencies, more energy is lost through the open end and port resonances become more damped with a broader, lower amplitude response. [10 p. 473]

Radiation Impedance – Piston Model

Acoustic radiation that arises from a moving surface is well understood and discussed in literature. To model the effects of a plane wave leaving a sensor port that encounters a surrounding medium, piston vibration theory is studied. A damped harmonic oscillator model can be used to represent the acoustic radiation as the impedance of a pressure wave exiting the flanged sensor port.

For the sensor port application, the reaction force of the surrounding fluid back onto a driving piston is first analyzed. [2 pp. 457-460, 3 pp. 184-187, 10 pp. 381-387] The configuration is flanged and the piston is assumed to be circular and rigid. It can be shown that if a force is applied to some device (or fluid parcel), that this applied force divided by the velocity of the device (or fluid parcel) represents the sum of the input mechanical impedance plus the mechanical impedance of the device (or fluid parcel). For the piston model, the force applied by the piston similarly encounters the sum of the piston mechanical impedance and radiation impedance of the propagated acoustic wave.[3 pp. 184-185] The radiation impedance, or mechanical impedance of the fluid parcel, can be obtained generally by using eq. (54), noting the overbar arc to denote mechanical impedance. It is represented by the complex reaction force divided by complex velocity at the point where the force is applied. The differential df_r' is the normal component of the piston reaction force locally on an area element dS, and u' is the normal component of velocity that in general may vary radially.[3 p. 184] Both the force term and velocity term are oscillatory functions of time.

$$\breve{Z}_{rad} = \int_S \frac{df_r'}{u'} \tag{54}$$

A force balance of an oscillating piston within a fluid can be represented as a damped harmonic oscillator given as eq. (55), where the left-hand-side represents the diaphragm motion (m is diaphragm mass, $\breve{R}_m$ is diaphragm mechanical resistance, and s is diaphragm stiffness), and f_p' is the externally applied force. [3 pp. 184-185, 11 pp. 180-181]

$$mx_{tt}' + \breve{R}_m x_t' + sx' = f_p' - f_r' \tag{55}$$

For a piston representing plane waves, the diaphragm is regarded as maintaining radial uniformity, where $u' = \overline{u}_x e^{i\omega t}$. With uniform movement, the reaction force, f_r', can then be reduced using eq. (54) and expressed in terms of the radiation impedance as $f_r' = \breve{Z}_{rad} u'$.

The solution to eq. (55) can be written in terms of the piston velocity as eq. (56). The radiation impedance, $\breve{Z}_{rad}$, is expanded into the real part, $\breve{R}_{rad}$, as the radiation resistance and imaginary part, $\breve{X}_{rad}$, as the radiation reactance.[11 p. 192]

$$u' = \frac{f_p'}{\breve{R}_m + i\left(\omega m - s/\omega\right) + \breve{Z}_{rad}} = \frac{f_p'}{\left(\breve{R}_m + \breve{R}_{rad}\right) + i\left(\omega m - s/\omega + \breve{X}_{rad}\right)} \tag{56}$$

For this harmonic oscillator model, an added mass can be used as a basis for a correction at the end of the port. The radiation reactance can be represented as an added mass by comparing the radiation reactance to the mass term in the imaginary part of the denominator. More precisely, this can be deduced by equating the piston velocity general solution, eq. (56), to the velocity solution of a simple forced harmonic oscillator, i.e., eq. (56) with $\breve{Z}_{rad} = 0$ since there is no reaction force. By comparison, it can then be observed that the radiation reactance contributes to an overall effective mass for a simple forced harmonic oscillator, i.e., $\omega m_{eff} \equiv \omega m + \breve{X}_{rad}$. The added mass, m_{rad}, can be written as the overall effective mass minus the piston diaphragm mass, $m_{rad} = m_{eff} - m$, or simply as eq. (57). The radiation reactance can therefore be considered individually as contributing as an added mass.

$$m_{rad} = \overline{\rho} A \Delta L = \frac{\breve{X}_{rad}}{\omega} \tag{57}$$

This added mass term has the effect of decreasing the resonance frequency.[3 p. 185] The mass is equivalent to that of an imaginary cylinder of ambient fluid having the same radius as the piston and length given by the end correction, ΔL.[11 p. 181] The wave encounters, not a zero load, but an effective load equivalent to a short continuation of the sensor port.[2 pp. 151-152] Note that the short continuation is referred to as 'effective height' when referring specifically to the piston model.

The radiation impedance that is represented in eq. (56) can next be obtained by analyzing the acoustics generated in the near field. The radiation impedance due to a circular piston can be expressed in a closed form developed in literature as eq. (58), where J_1 is the first order Bessel function of the first kind and H_1 is the first order Struve function.[2 pp. 151, 457-460, 3 pp. 185-187]

$$\breve{Z}_{rad} = \breve{R}_{rad} + i\,\breve{X}_{rad} = \overline{\rho c} A \cdot \left[\left(1 - \frac{J_1(2kR)}{kR}\right) + i\left(\frac{H_1(2kR)}{kR}\right)\right] \tag{58}$$

Equation (59) and eq. (60) are the real and imaginary bracketed part of eq. (58), which are known as piston functions. They can be thought of as a normalized specific acoustic impedance, normalized by $\overline{\rho c}$, where $x = 2kR$.

$$R_1(x) = 1 - \frac{2J_1(x)}{x} \tag{59}$$

$$X_1(x) = \frac{2H_1(x)}{x} \tag{60}$$

Figure 6 shows a plot of the piston resistance function, $R_1(x)$, and the piston reactance function, $X_1(x)$.

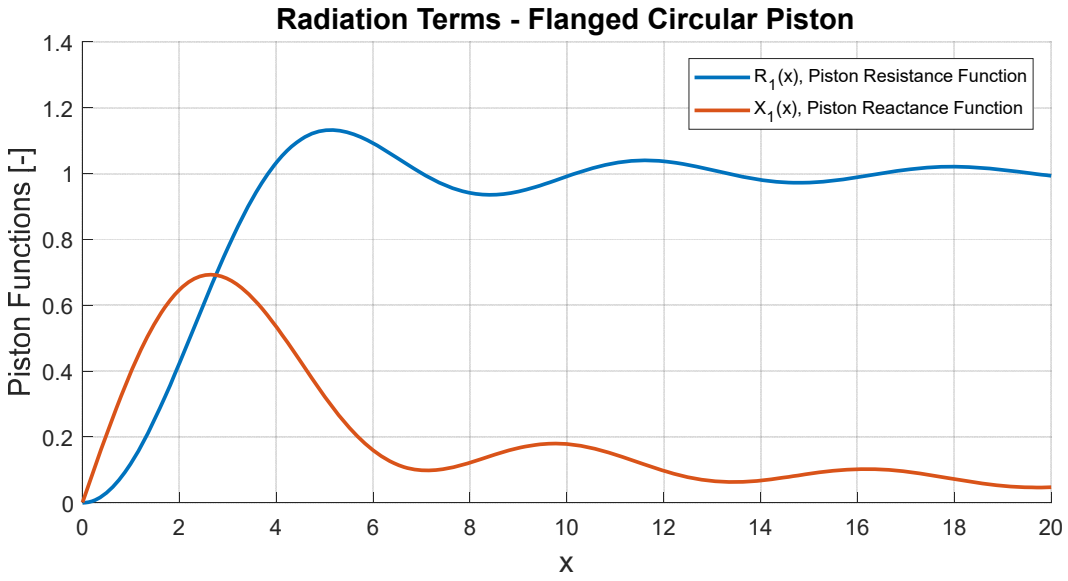

Figure 6. Radiation Terms for a Flanged Circular Piston

As described earlier, the open end of the sensor port can be represented with this piston model. At the sensor port opening, a propagating wave leaving the sensor port confronts a sudden increase in total resistance, described by the resistance term in eq. (58), and an increase in mass loading, described by the reactance term in eq. (58). The radiation reactance is positive and represents an added mass that results in an overall decrease in resonant frequency. The added mass to the sensor port is referred to as the radiation mass.[3] p.185

The radiation mass contribution is examined first. Equation (57) can be rewritten as eq. (61) in terms of the short continuation.

$$\Delta L = \frac{\breve{X}_{rad}}{\bar{\rho} A \omega} \tag{61}$$

Equation (61), is referred to as the end correction, and can now be rewritten in terms of the piston reactance function using eq. (58) and noting $\breve{X}_{rad} = \bar{\rho}\bar{c}A \cdot X_1(2kR)$. It can subsequently be written in terms of the Struve function noting that $X_1(2kR) = H_1(2kR)/kR$ from eq. (60). The end correction in terms of the piston reactance function or Struve function is given as eq. (62). This end correction is derived for a flanged oscillating piston, however it is a good representation of an oscillating planar wave at a sensor port opening.[2] pp. 151-152

$$\Delta L = \frac{X_1(2kR)}{k} = \frac{H_1(2kR)}{k^2 R} \tag{62}$$

Equation (62) reveals that the end correction is in fact frequency dependent and a precise model would incorporate this dispersion. The well-known end correction, eq. (2), can be estimated by characterizing the low frequency limit. To obtain this approximation, eq. (59) and eq. (60) are written as a formal Maclaurin power series in eq. (63) and eq. (64).

$$R_1(x) = 1 - \frac{2J_1(x)}{x} = \sum_{m=0}^{\infty} \frac{(-1)^m}{\Gamma(m+2)\Gamma(m+3)} \left(\frac{x}{2}\right)^{2m+2} = \frac{x^2}{2 \cdot 4} - \frac{x^3}{2 \cdot 4^2 \cdot 6} + \frac{x^5}{2 \cdot 4^2 \cdot 6^2 \cdot 8} - \cdots \tag{63}$$

$$X_1(x) = \frac{2H_1(x)}{x} = \sum_{m=0}^{\infty} \frac{(-1)^m}{\Gamma\left(m+3/2\right)\Gamma\left(m+5/2\right)} \left(\frac{x}{2}\right)^{2m+1} = \frac{4}{\pi}\left(\frac{x}{3} - \frac{x^3}{3^2 \cdot 5} + \frac{x^5}{3^2 \cdot 5^2 \cdot 7} - \cdots\right) \quad (64)$$

The linearization of the expansion near $x = 0^+$ is given as the first term in eq. (64). This can be visualized as a linear approximation to the Figure 6 exact solution in the low frequency limit, where $2kR \ll 1$. The low frequency approximation is given as eq. (65).

$$X_1(x) \approx \frac{4x}{3\pi} \quad (65)$$

This low frequency approximation can be applied to eq. (62), where $x = 2kR$ to give the well-known effective length end correction as eq. (66). At low frequency, the piston appears to be loaded with a cylindrical volume of fluid whose cross-sectional area is πR^2 and end correction is given by eq. (66).[3 p. 187] Note that the end correction for this low-frequency approximation is not frequency dependent.

$$\Delta L \approx \frac{8R}{3\pi} \quad (66)$$

In many cases for the fundamental mode, the error is small in using eq. (66), however, for precise calculations in all port configurations and at higher frequencies, the exact formula in eq. (62) is recommended. References [**12, 13**] discuss efficient approximations for the Struve function since eq. (63) and eq. (64) become increasingly difficult to evaluate, which may be necessary to achieve a small relative error. An end correction comparison between the exact solution and approximate solution is shown in Figure 7 for an example sensor port with radius 0.25 inches and ambient air.

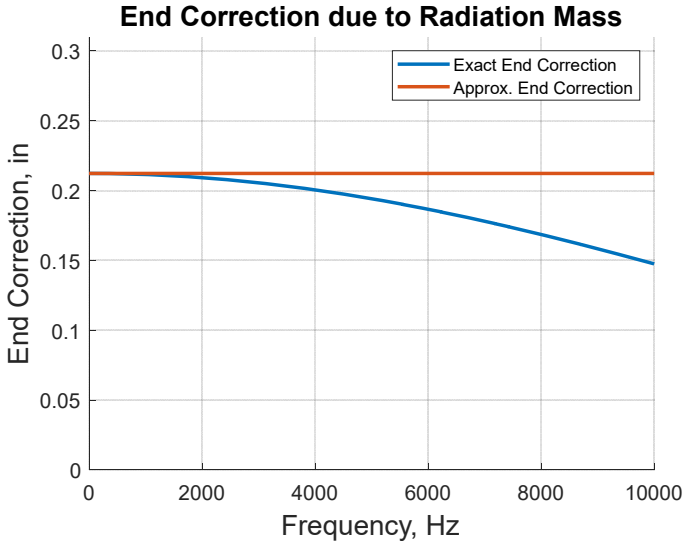

Figure 7. Exact and Approximate End Correction: Ambient Air (c=1140 ft/sec) and 0.25 inch Radius

The radiation resistance contribution is examined next. For the simple harmonic oscillator model described in eq. (55), the temporal absorption coefficient for the radiation mechanism, $\tilde{\beta}_{rad}$, is given as eq. (67). [3 pp. 8-11, 17, 184-185] The tilde denotes that the parameter is not related to the phase shift parameter, β, used throughout the paper. The temporal absorption coefficient parameter is commonly written in terms of damping ratio and undamped natural frequency as $\tilde{\beta} \equiv \zeta\omega_n$.

$$\tilde{\beta}_{rad} = \frac{\breve{R}_{rad}}{2m_{rad}} \tag{67}$$

Both the temporal absorption coefficient and the spatial absorption coefficient can be used to describe the amplitude decay of a pressure wave. The temporal absorption coefficient can be transformed into the spatial absorption coefficient using the following relationship. **2** pp. 299-300, **3** pp. 8-11, 17, 212, 217, 285

$$\tilde{\beta}_{rad} = \overline{c}\alpha_{rad} \tag{68}$$

Substituting eq. (68) into eq. (67) and using eq. (57) gives the form of the spatial absorption coefficient representing the radiation mechanism.

$$\alpha_{rad} = \frac{k}{2}\frac{\breve{R}_{rad}}{\breve{X}_{rad}} \tag{69}$$

Substituting the resistance and reactance terms of eq. (58) into eq. (69) and using the relationship in eq. (62) gives a useful form of the absorption coefficient. The spatial absorption coefficient associated with radiation impedance can be written as eq. (70), considering that the acoustic radiation from the flanged port behaves as the pressure field generated by a flanged piston. Note that an accurate representation of the end correction is given as eq. (62).

$$\alpha_{rad} = \frac{1}{2\Delta L}\cdot\left(1 - \frac{\overline{c}\cdot J_1(2\omega R/\overline{c})}{\omega R}\right) \tag{70}$$

The end correction length is a characteristic dimension or artificial length that describes the additional mass of fluid necessary to simulate the radiation impedance. The radiation contribution associated with the harmonic oscillator at the opening location is embedded entirely in the absorption coefficient. As such, the propagation of a pressure response associated with the reaction to an oscillating piston is simulated with the lossless fluid (no thermoviscous dissipation) outside of the port over the length of the end correction. The phase speed is therefore simply the fluid sound speed over the span of the end correction, $c_{p,rad} = \overline{c}$. Noting that the phase shift parameter can be written using eq. (16), the propagation constant for the radiation mechanism can be described using eq. (71).

$$\hat{\gamma}_{rad} = \alpha_{rad} + i\beta_{rad} = \frac{1}{2\Delta L}\cdot\left(1 - \frac{\overline{c}\cdot J_1(2\omega R/\overline{c})}{\omega R}\right) + i\frac{\omega}{\overline{c}} \tag{71}$$

Expanding this equation using the accurate definition of the end correction gives the propagation constant for acoustic radiation explicitly as eq. (72).

$$\hat{\gamma}_{rad} = \frac{R\omega^2/\overline{c}^2}{2H_1(2\omega R/\overline{c})}\cdot\left(1 - \frac{\overline{c}\cdot J_1(2\omega R/\overline{c})}{\omega R}\right) + i\frac{\omega}{\overline{c}} \tag{72}$$

The propagation constant described here for acoustic radiation effects is a critical advancement for application to sensor ports. Depending on the sensor port configuration, the influence of radiation acoustics can be significant.

NUMERICAL MODELING

A primary advantage of a computer simulation, or numerical modeling, is to tackle problems that are too complex for analytical solutions. However, it is also a very useful approach in gaining insight into relevant physical mechanisms and important system features. Tools such as COMSOL Multiphysics[14] and the ANSYS software suite are two of the more well-known engineering multiphysics software tools. These tools provide a simple work flow and user interface, integrate and numerically simulate coupled physical models, and provide a means to manage solution data and visualize results. The examples and procedures in this document will use COMSOLversion 5.4 as the numerical modeling tool.

While the sensor port analytical models are relatively simple and efficient, they are tractable because assumptions are enforced and limitations exist. In many cases, the limitations may not be relevant and the solution is representative – but there are situations where more complex physics must be included. By using COMSOL, many of these limitations can be addressed in a rigorous manner. There are several examples of limitations that may be relevant to a sensor port analysis that are not usually incorporated in an analytical model. These include the effects of crossflow over the sensor port opening, flow through the sensor port, finite and realistic geometry – such as a port installed in a pipe rather than in an infinite medium, thermal conditions surrounding the sensor port, nonlinear finite acoustics, unsteady losses at geometric interfaces, accurate property distribution in the ambient surroundings and port geometry, fluid-structural interaction, and true dynamic behavior of the fluid system (rather than using a piston model as an approximation).

Aside from the removal of physical and geometric limitations, there is another very important advantage in using a numerical framework for sensor port analysis. A direct comparison can easily be made by comparing the solutions of the exact configuration (with a sensor port) and the desired configuration (usually with no sensor port). Often it is desired to remove the effects of the sensor port or understand what the port influence is to help determine the acceptable response range. This can be addressed by simulating the exact configuration and the desired configuration separately using all of the identical simulation conditions, e.g., same excitation source and same boundary conditions. Because the numerical simulation is deterministic, the pertinent quantities of interest between the two configurations can be obtained very precisely. The theory for this comparative analysis is developed and described throughout. This innovative yet very basic procedure is remarkably powerful when combining solutions from deterministic numerical simulations.

Computer simulations have many advantages, however there are some disadvantages. Depending on the additional physics and domain included, the computation can be extremely time intensive. However, computer speed and numerical algorithms are always improving. Additionally, one difficult part of computer simulation is often the model setup, however COMSOL's work flow is designed so that the setup difficulty is minimized.

Numerically Modeling Piston Functions

In this section, the piston functions that are discussed previously theoretically are modeled numerically by solving the Helmholtz equation in the frequency domain. This is done by using the COMSOL *Pressure Acoustics, Frequency Domain* interface. This interface is suited to model pressure variations for the propagation of acoustic waves in fluids at quiescent background conditions.[15] This simple numerical example is a very important step in the sensor port analysis. Most importantly, it provides a verification that relevant radiation acoustics physics can be modeled adequately.

Equation (58), shows that both the fluid properties and the radius influence the piston functions and radiation impedance. Therefore, for a typical verification analysis, the piston radius would be set equal to the sensor port opening radius and the fluid properties would also be the same. Satisfactorily simulating the piston functions over the sensor port frequency range of interest ensures that the radiation acoustics will be captured adequately in a sensor port with the same radius and fluid. Considering that

the sensor port response will be studied using the same setup, addressing regions of large error in the numerical piston model can help determine optimal domain and mesh designs for use in the sensor port analysis. To satisfactorily model the radiation impedance in the sensor port model, both the domain and mesh need to be designed appropriately.

Example Flanged Circular Piston

The acoustics associated with an oscillatory piston of radius 0.25 in (0.00635 m) is studied in ambient air. The air is at a temperature of 77 °F (298.15 K) with sound speed 1136 ft/s (346 m/s) and density 4.2779E-5 lb_m/in^3 (1.1841 kg/m^3). The total domain radius is 7.5 in (0.1905 m), which is 30x the piston radius, and includes a 0.375 in (0.009525 m) thick perfectly matched layer (PML) that behaves as an absorptive boundary. A grid refinement region is also defined at 10x the piston radius near the far field transition radius. The analysis is explored over the bandwidth through 20,000 Hz by increments of 200 Hz. The minimum wavelength of interest, an important parameter for mesh resolution, is therefore 0.6816 in (at 20,000 Hz).

Domain Setup

Figure 8 shows the general domain setup for numerically modeling the piston functions. The domain is designed using a 2-D axisymmetric model where the vertical axis is the axis of symmetry.

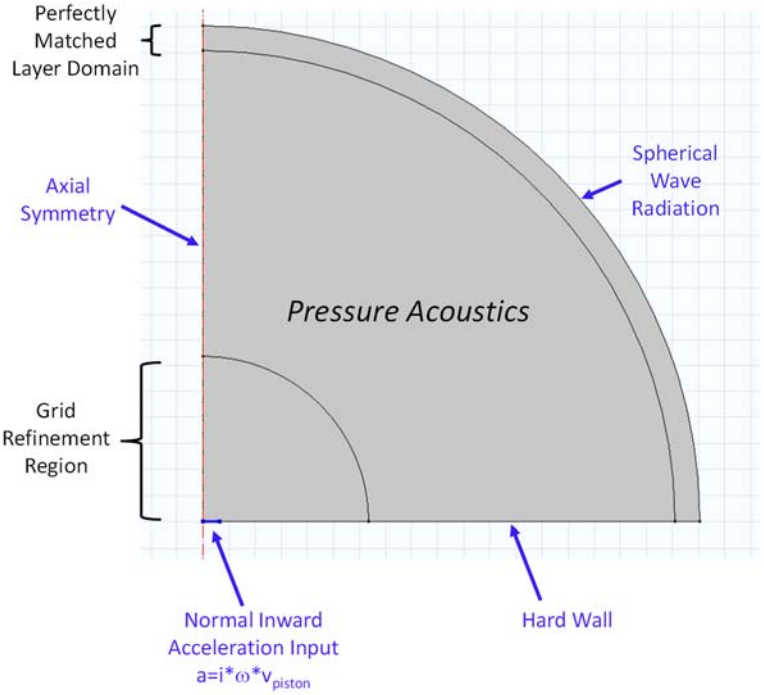

Figure 8. Modeling Piston Functions – 2-D Axisymmetric Domain Setup

The piston is defined as a horizontal radius (blue) in the lower-left part of the domain with an inward normal acceleration. The acceleration can be represented as $a = i \cdot \omega \cdot v_{piston}$ given the piston velocity, v_{piston}. A constant velocity amplitude is imposed and set at 1 m/s. Any value for the piston velocity is acceptable as this is a linearized model and impedance calculations consider both the input and response.

Except for the piston radius, the rest of the horizontal axis is defined as a sound hard (closed) boundary where the normal component of acceleration (and velocity) is zero. This definition is consistent with the hard wall definition used for a flanged baffle.

The piston functions are estimated for a piston set in a plane baffle of infinite extent. An ideal PML absorbs all outgoing waves without causing spurious reflections and would represent the infinite extent. A sensitivity study for this problem showed that the PML could acceptably resolve the acoustic response down to a minimum frequency that has a wavelength approximately 10x longer than the domain radius. Other considerations may come into play in the design of the overall domain size and error should always be reviewed because of unique aspects of a particular problem.

Mesh Design

A major source of error can arise by inadequately resolving the mesh. One particular area of interest should be the vicinity of the piston where the surface pressure and reaction force must adequately be resolved. Consider that the pressure produced by the piston results from a continuum of flanged simple sources that radiate spherically.[3 pp. 172, 179] Across the entire surface of the piston, each infinitesimal area produces an incremental pressure.[3 p. 185] And for a very short piston radiation wavelength, where $kR \gg 1$, each portion of the surface radiates separately and is separately loaded.[10 pp.385-386] A refinement of 100 grid points across the piston provided a diminishing return in error over the range of wavelengths examined. As these additional grid points are only needed across the piston, the computational expense is not greatly increased.

An arc at 10x the piston radius is defined that encompasses a grid refinement region, and is shown in Figure 8. This region is used for a more refined mesh in order to better resolve the nearfield radiation effects. This region is loosely based on the characteristic farfield transition distance which can be inferred considering $r \gg R$ and $r \gg kR^2$.[16 p. 225] Selecting the widest of these two ranges is more conservative than using the Rayleigh distance, which marks the transition from nearfield to farfield, defined in reference [**2**] as $r \gg kR^2/2$. Reference [**17**] provides a thorough review on various other definitions of the nearfield and farfield transition distance. For this example, a free triangle mesh in this refined region was specified using a size expression such that the elements were no larger than the smaller of two values: 6x smaller than the piston radius or 30x smaller than the minimum wavelength. In the courser region, the free triangle mesh was also based on the smaller of two values: 4x smaller than the piston radius or 20x smaller than the minimum wavelength. In this example, the maximum frequency is 20,000 Hz, and therefore the smaller wavelength-based definition is used for the mesh. These definitions are loosely based on sensitivities that show an acoustic wavelength can be resolved with approximately five elements, but also to ensure good element transition from the higher refined regions to the lower refined regions. In addition, while not systematically studied, the increased mesh refinement region was implemented to capture interference and directivity attributes in the nearfield.

Comparison of Numerical and Analytical Solution

A piston function comparison between the numerical COMSOL solution using the domain and mesh previously described and exact analytical solution is shown in Figure 9. The exact curves for the piston resistance function and piston reactance function can be plotted as a function of frequency using eq. (59) and eq. (60), respectively. In COMSOL, eq. (54) can be used directly to estimate the numerical value of the impedance; and subsequently the piston functions can be estimated from the real and imaginary part (and normalized by $\overline{\rho c} A$). The functions shown in eq. (73) and eq. (74) can be estimated numerically using COMSOL to obtain the piston resistance function and the piston reactance function, respectively. The density and sound speed are directly used in the evaluation, however their effect on amplitude is canceled by the evaluation of the integral term. This can be observed by comparing eq. (54),

eq. (58), eq. (59), and eq. (60). This evaluation is performed at each frequency to numerically produce the curves in Figure 9.

While *normalized* piston functions apply for any circular piston in any fluid, the geometry and properties are noted on the figure used to numerically produce the curves.

$$R_1 = \frac{1}{\overline{\rho c}\,\pi R^2} \cdot \Re\left(\int_0^{2\pi} \int_0^{R} \frac{p(r)}{v_z(r)} r\, dr d\theta \right) \tag{73}$$

$$X_1 = \frac{1}{\overline{\rho c}\,\pi R^2} \cdot \Im\left(\int_0^{2\pi} \int_0^{R} \frac{p(r)}{v_z(r)} r\, dr d\theta \right) \tag{74}$$

While the normalized form is plotted analytically in Figure 6, plotting at each frequency in Figure 9 shows the piston function contribution for a typical sensor port.

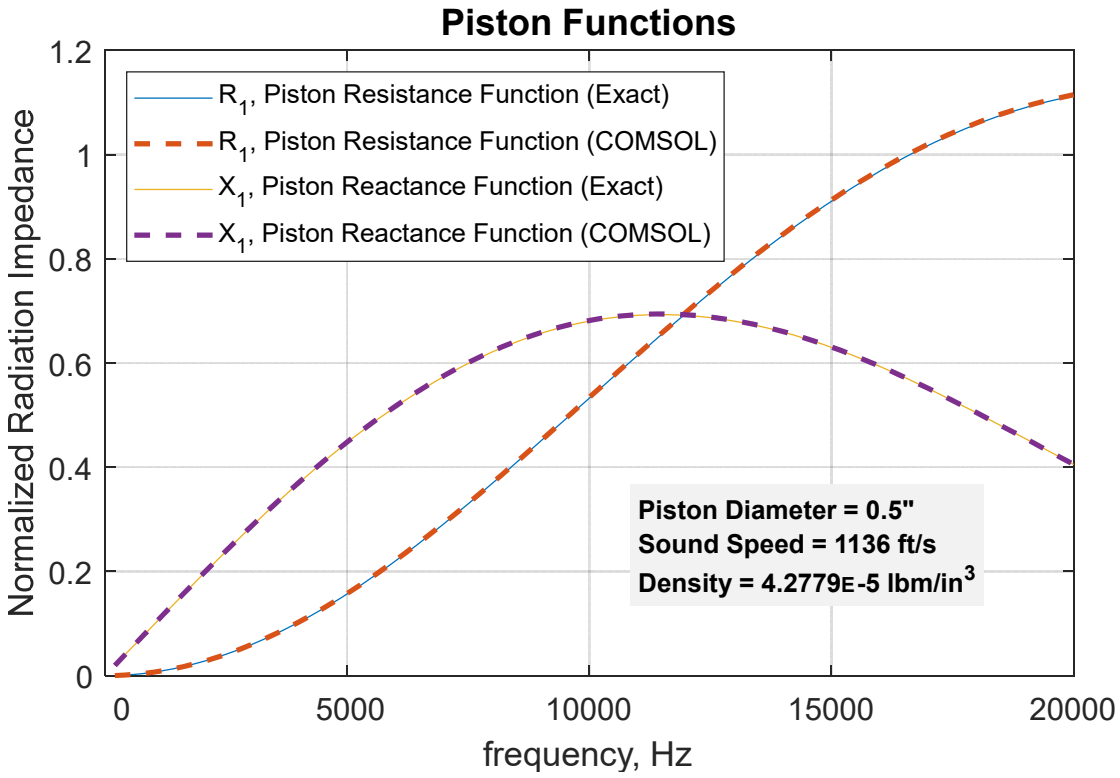

Figure 9. Piston Functions as a Function of Frequency for a 0.5 in Diameter Piston in Ambient Air

Figure 10 shows the effective piston height as a function of frequency. As discussed previously, the piston appears to be loaded with a cylindrical volume of fluid whose cross-sectional area is πR^2 and height given by the exact curve in Figure 10.[3 p. 187] This is equivalent to applying an end correction to a sensor port. The exact curve for a flanged piston can be plotted using eq. (62) and the approximate solution is from eq. (66). It was shown previously that the end correction is related to the imaginary part of the impedance and can be obtained numerically. In COMSOL, eq. (61) can be used directly to estimate the numerical value of the effective height by incorporating the radiation reactance from eq. (54). At each frequency, the function shown in eq. (75) can be evaluated.

$$\Delta L = \frac{1}{\bar{\rho}\omega\pi R^2} \cdot \Im\left(\int_0^{2\pi} \int_0^{R} \frac{p(r)}{v_z(r)} r \, dr d\theta \right) \tag{75}$$

Figure 10 shows that for a piston, the exact effective height solution compares identically to the numerical solution. The approximate solution compares well only at low frequencies.

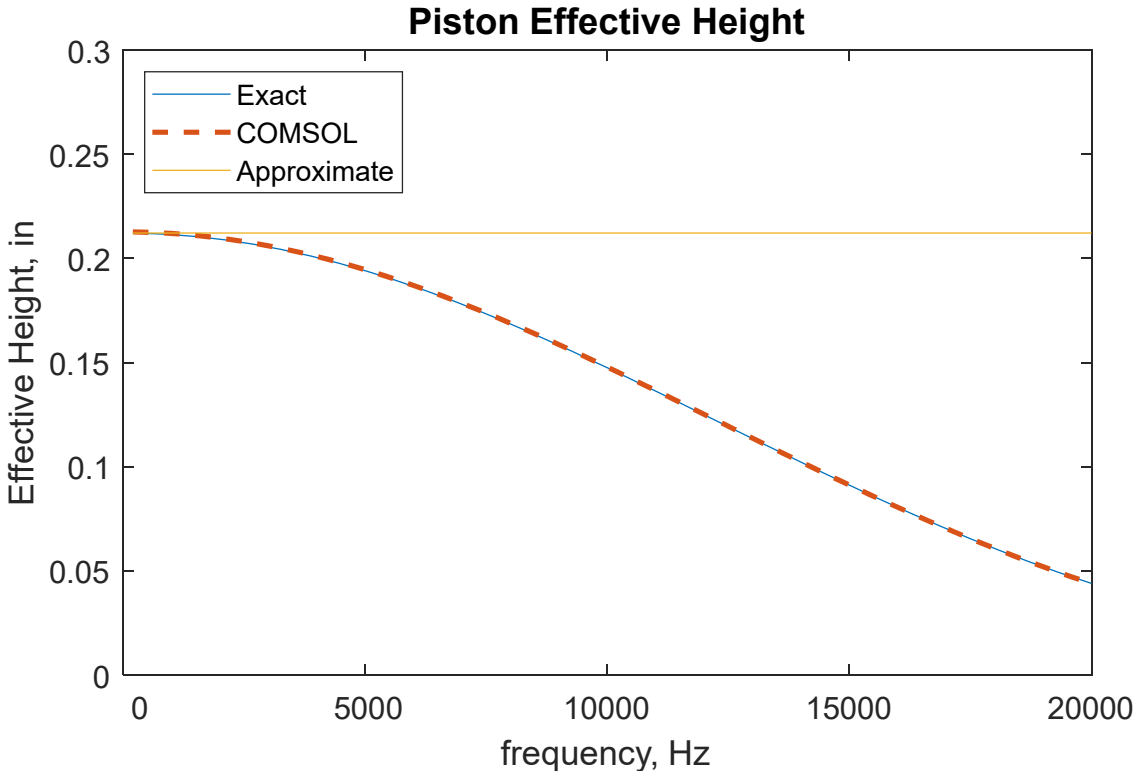

Figure 10. Piston Effective Height as a Function of Frequency

Numerical Analysis of Thermoviscous Boundary Dissipation

In the previous section, a piston model was analyzed to verify the radiation acoustics physical mechanism and also to aid in domain and mesh design of the forthcoming sensor port simulation. In this section, the thermoviscous boundary dissipation previously discussed theoretically is modeled numerically and analytically in several different ways. Three separate numerical approaches using COMSOL are first compared. Four separate analytical models are also compared. The comparisons are made to understand and explore differences. Table 1 summarizes the different thermoviscous models in increasing order of accuracy.

Table 1. Numerical and Analytical Models of Thermoviscous Boundary Dissipation

Model	Type	Domain	Description
Heuristic	Analytical	Frquency Domain	Helmholtz equation with propagation constant from heuristic model
Traditional	Analytical	Frquency Domain	Helmholtz equation with approximate propagation constant from physical model
Exact – with 1st Order Approximation	Analytical	Frquency Domain	Helmholtz equation with approximate propagation constant from physical model
Exact	Analytical	Frquency Domain	Helmholtz equation with exact propagation constant from physical model
Narrow Region Acoustics	Numerical	Frquency Domain	Helmholtz equation with exact propagation constant from physical model
Thermoviscous Acoustics	Numerical	Frquency or Time Domain	Navier -Stokes with continuity and energy that has been linearized
Multiphysics	Numerical	Time Domain	Coupled laminar flow and fluid heat transfer - full Navier Stokes with continuity and energy

The first numerical approach listed is the 'Narrow Region Acoustics' model. In this method, the Helmholtz equation is solved numerically in the frequency domain, and a complex wave number that is described by a boundary layer dissipation theoretical model is applied to the numerical

framework.[2] pp. 324-325, [15] In fact, COMSOL uses the exact form of the complex wave number described by eq. (37) in its numerical framework. This approach effectively is a quasi- one-dimensional model where the dissipation is distributed evenly within the fluid everywhere in the port. The 'Narrow Region Acoustics' model is implemented by using the COMSOL *Pressure Acoustics, Frequency Domain* interface and adding a COMSOL node called *Narrow Region Acoustics*. This model has a very low computational cost compared to the more accurate 'Thermoviscous Acoustics' and 'Multiphysics' models, but is not accurate in all scenarios such as for short, high-aspect ratio ports or ports that do not have a constant cross section.[15] The numerical approach is equivalent to using the 'Exact' analytical model where the propagation constant is derived from the exact thermoviscous model described previously as eq. (51).

The second numerical approach is referred to as the 'Thermoviscous Acoustics' model and in general is an improvement in accuracy. This model uses the linearized Navier-Stokes equations with quiescent background conditions including continuity and an energy balance. It can be applied in the frequency domain or time domain, but is studied here in the frequency domain, using the COMSOL *Thermoviscous Acoustics, Frequency Domain* interface. This interface is suited to model pressure, velocity, and temperature variations for the propagation of acoustic waves with quiescent background conditions near walls where viscous and thermal boundary layers exist.[15]

The third numerical approach, referred to as the 'Multiphysics' model is the most accurate and solves the complete Navier-Stokes equations including continuity, along with the convective-diffusion energy equation (including sources). The 'Multiphysics' model can be applied only in the time domain, by manually coupling COMSOL's *Laminar Flow* interface with its *Heat Transfer in Fluids* interface. This multiphysics interface is suited to model pressure, velocity, and temperature variations and can be extended to more complex cases such as finite-amplitude (nonlinear) waves, propagation in liquids, or acoustics with flow. The 'Multiphysics' model is similar to frameworks used in traditional computational fluid dynamics (CFD) and simulates both the flow effects and heat transfer in the fluid. One important contribution incorporated in the energy balance is associated with the pressure work. The work done by changes in pressure, including heating through adiabatic compression, is discussed in reference [**18** pp. 336-337] where the energy change equation for a fluid is placed in the form of temperature.

The analytical models listed in Table 1 are similar to the 'Narrow Region Acoustics' numerical model, where the Helmholtz equation (or time-independent wave equation) is solved using a propagation constant that describes the thermoviscous dissipation. The analytical models only differ by applying separate propagation constants, which are dependent on the particular boundary layer dissipation theoretical model and approximation made. The most accurate analytical propagation constant for boundary layer dissipation is given as eq. (51) and referred to as the 'Exact' model. A 1st order approximation to the exact solution is occasionally used, and described in reference [**2** p. 325], and referred to as the 'Exact – with 1st Order Approximation' model. The traditional approach is to use eq. (42) and is referred to as the 'Traditional' model. Lastly, the 'Heuristic' model, described in reference [**8**] is an approximation analogous to a damped SDOF system and considers heuristically that there is a general pressure drop per unit length associated with thermoviscous effects.

In this document, the analytical framework uses a pressure transfer equation model and is derived from the wave equation. For comparisons in this section, the analytical solutions use the eq. (26) transfer equation for a 1-line model and incorporate a propagation constant based on one of the four separate analytical models.

The analysis in this section provides verification that the physics associated with thermoviscous dissipation, i.e. acoustic boundary-layer dissipation, is modeled adequately and will be adequately applied to the forthcoming sensor port analysis. To model the acoustic boundary-layer dissipation satisfactorily within the sensor port, both the domain and mesh need to be designed appropriately.

Numerical Model Example – Thermoviscous Boundary Dissipation

The response associated with a port of radius 0.25 in (0.00635 m) and length of 5 in (0.127 m) is numerically studied in ambient air at a temperature of 77 °F (298.15 K).

Domain Setup

The domain setup is described for the 'Thermoviscous Acoustics' model. Differences in domain setup are also noted for 'Narrow Region Acoustics' and 'Multiphysics' models. Figure 11 shows the general domain setup for numerically modeling the dissipation effects associated with the acoustic boundary layer in a 1-line port model. The domain is designed using a 2-D axisymmetric model where the vertical axis with the dashed red line is the axis of symmetry.

To model the frequency response function (also referred to as the transfer function in this paper) of the port, the concept of input impedance is applied. The input impedance, or driving-point impedance, is the system equivalent impedance that is seen by an external source. The input impedance is a measurement of impedance at one location, but describes the spatial wave propagation through the entire system. Therefore a transfer function can be obtained by applying an external source at one end of the port, followed by measuring the input response at the driven end and the output response at the other end of the port.[3 pp. 281-283] To apply a source that behaves as an open (soft) boundary, the external source should be applied as a massless driver with no stiffness.[3 pp. 281-283] In COMSOL, a massless driver with no stiffness can be applied simply by using a prescribed velocity at one end as shown in Figure 11. Using this approach, the resulting pressure transfer function can simply be probed. This general approach is used to obtain lumped models for acoustic elements, such as short cavities, Helmholtz resonators, and more complex acoustic networks.[2 pp. 144-150, 153-156, 3 pp. 280-286] A constant velocity amplitude is imposed and set at 1 m/s. However, any value for the prescribed velocity is acceptable as the transfer function calculations consider both the input and response for the linearized model.

Note that in the 'Multiphysics' model, a velocity amplitude of 1E-5 m/s is applied since the model is not linearized and input amplitudes do play a role. This velocity input produced a maximum pressure near 0.004 Pa, which is well within the acoustic regime. The input impedance concept does not apply for the time domain model.

The port walls behave effectively as an infinite heat source or sink and can be modeled as an isothermal boundary.[2 p. 323] In the fluid mainstream, the compressions and expansions take place adiabatically.[2 p. 323] The driver location represents the open end of the port in the mainstream of the fluid, so an adiabatic condition best approximates the thermal condition at this boundary. There would be no heat transfer to a wall at this boundary and the temperature would not be constrained. Sensitivities show that the thermal boundary condition of the acoustic driver has a negligible effect on results.

The remainder of the domain consists of an axis of symmetry and hard walls as shown in Figure 11.

While Figure 11 shows the general domain setup for numerically modeling the dissipation effects associated with the acoustic boundary layer for the 'Thermviscous Acoustics' model, the domain setup for the 'Narrow Region Acoustics' model is very similar to the setup shown in the figure except that it has no thermal boundary conditions. The COMSOL *wide duct approximation* selection allows the model to apply analytical propagation constants that account for thermoviscous dissipation.

The 'Multiphysics' model has a couple additional domain considerations. As noted previously, it uses the COMSOL *Laminar Flow* and *Heat Transfer in Fluids* physics interfaces. The first consideration is the differing nomenclature in the *Heat Transfer in Fluids* where the terms in Figure 11, *Adiabatic* and *Isothermal*, are referred to as, *Thermal Insulation* and *Temperature*, respectively. The more important interface characteristic is to ensure the variables in the *Heat Transfer in Fluids* interface work together with the variables in the *Laminar Flow* interface. To ensure this occurs, the *Fluid Properties* node in the

Laminar Flow interface and *Fluid* node in the *Heat Transfer in Fluids* interface must use the dependent variables. For example, the absolute pressure should be given as the instantaneous pressure, $p + p_0$, and the temperature as the instantaneous temperature, T, rather than using the global steady ambient conditions, p_0 and T_0. For the particular interface, p and T are the COMSOL dependent variables.

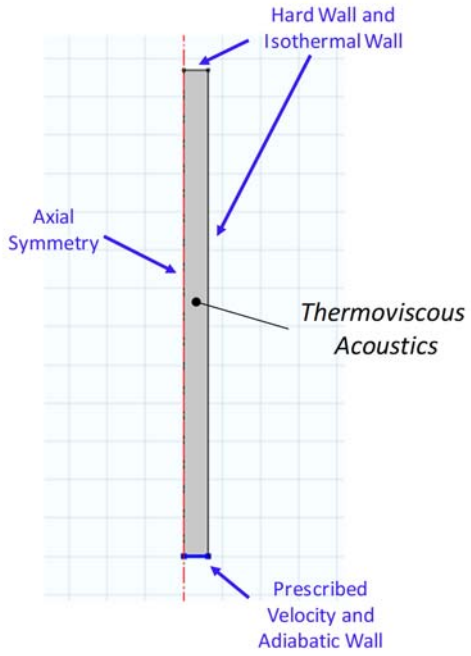

Figure 11. Modeling Thermoviscous Effects – 2-D Axisymmetric Domain Setup

Numerical Model – Mesh Design

For the Narrow Region Acoustic model, only typical acoustic considerations should be made regarding the mesh design as the dissipation effects are homogenized over all the elements. Generally, for this case, the number of elements needed is purely based on the number of elements needed to resolve an acoustic wavelength, i.e., approximately five elements.

For the 'Thermoviscous Acoustics' and 'Multiphysics' model, the primary mesh design requirement should address capturing the dissipation effects. Efforts should be made to ensure there are enough elements within the acoustic boundary layer. The minimum boundary layer thickness can be obtained by considering the highest frequency of interest and using eq. (35) and eq. (36), which define the viscous and thermal boundary layer thickness, respectively. It is recommended that a sensitivity study be performed to investigate the effect of element size on relative error.

Figure 12 shows the mesh for the 'Thermoviscous Acoustics' model in the vicinity of the boundary layer. Note that it includes a boundary layer mesh along the bottom boundary. A sensitivity was performed for this example and it was shown that the dissipation effect along this boundary is extremely small, but it was retained in general to account for minor corner effects where transverse flow may be present. Since this frequency domain model encompasses a wide frequency range, there is a range of acoustic boundary layer thicknesses shown with the blue and green bars on Figure 12. The overall mesh in this example comprises 31,992 quad elements and 32,751 mesh vertices. A mesh sensitivity study was performed showing that some coarsening is possible without producing discernable changes in results.

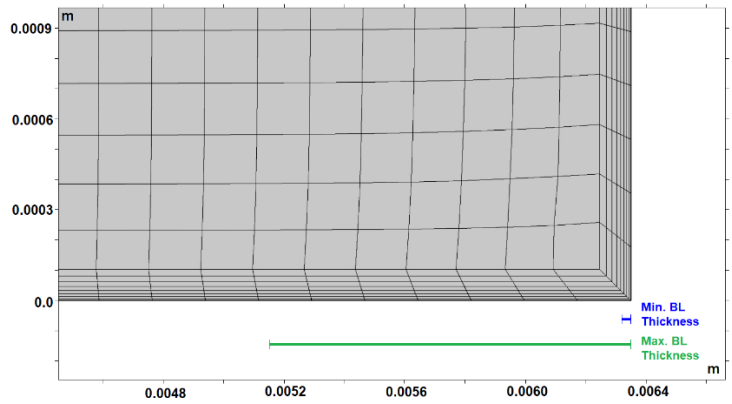

Figure 12. Mesh in the vicinity of the acoustic boundary layer. Blue and green bars show minimum and maximum boundary layer thicknesses, respectively. Note use of metric dimensions.

The overall mesh of the 'Multiphysics' model includes 8946 elements and 5740 mesh vertices with tri elements in the interior and quad elements for the boundary layer. Since the 'Multiphysics' model is simulated within the time domain, there are several additional considerations. The primary considerations are an appropriate solver such as the Generalized alpha time stepping method to minimize numerical damping and to also ensuring stationarity is reached.

Comparison of Numerical and Analytical Solution

A comparison between the numerical COMSOL solutions (except the 'Multiphysics' solutions) and analytical solutions are shown in Figure 13. The response curve of each shows that in general all of the models produce similar results for this example case.

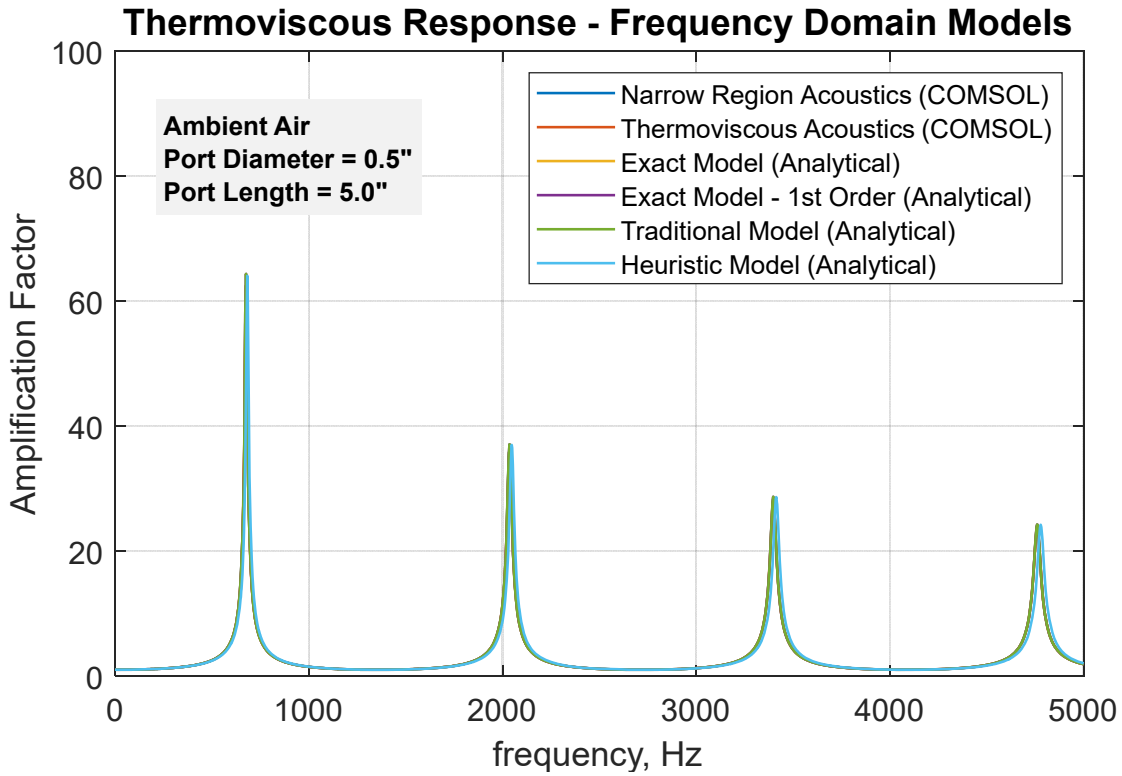

Figure 13. Thermoviscous Response for a Sensor Port

A detail zoomed-in view of the first mode is shown in Figure 14 for the analytical models ('Narrow Region Acoustics' computational model is included for comparison) and Figure 15 for the computational models.

Figure 14 shows that the COMSOL 'Narrow Region Acoustics' computational model and the analytical 'Exact Model' overlay exactly as expected since they both use an equivalent propagation constant. The 'Exact Model – with 1st Order Approximation' is very similar to the 'Traditional Model'. This is expected since the propagation constant has only a small difference in phase speed. The gain for these has a noticeable error when compared to the 'Exact' model, though, and is associated with limiting the series expansion of the propagation constant to first order. This error is also present in the 'Heuristic Model'. Additionally, the physics associated with the 'Heuristic Model' does not capture the appropriate thermoviscous boundary layer phase velocity and the error in frequency is evident.

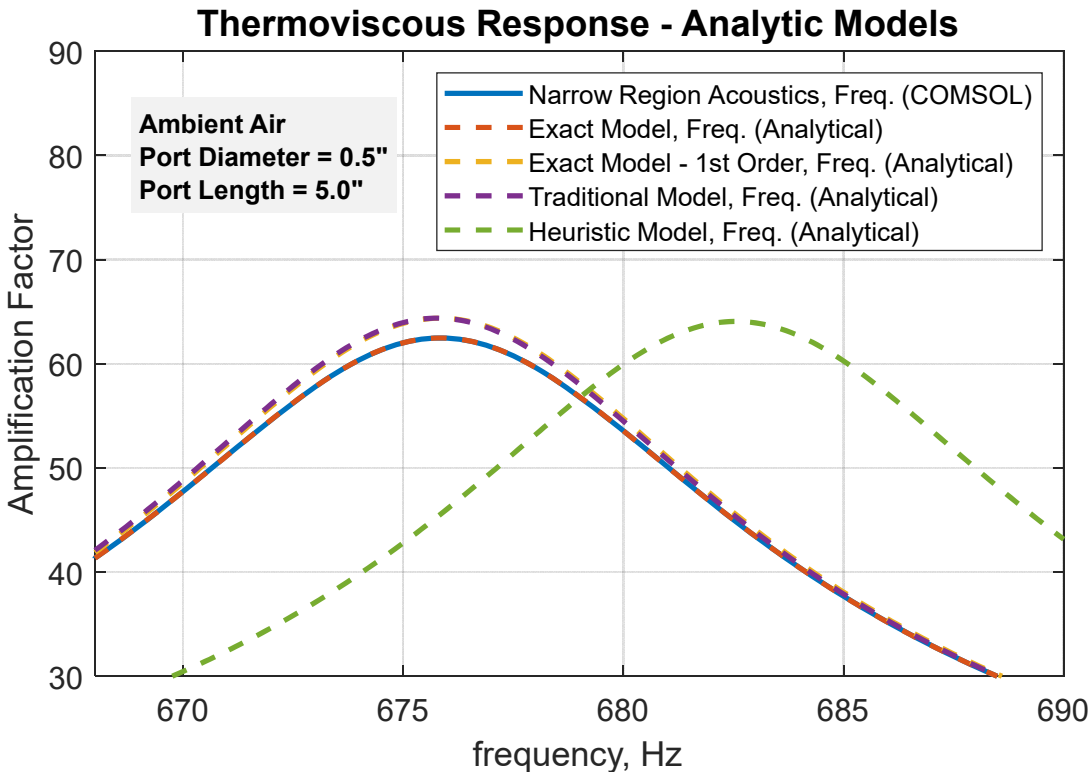

Figure 14. Thermoviscous Response for a Sensor Port – Analytical Models, Detailed View

In Figure 15, the computational models are compared. The 'Narrow Region Acoustics' model and the 'Thermoviscous Acoustics' model compare very closely. However, there is a small but noticeable difference between the 'Multiphysics' model and the other computational models. The 'Multiphysics' model incorporates the most complete set of equations that describe the thermoviscous acoustics phenomena, i.e., solving the Navier-Stokes equations and an energy balance directly, and accounts for additional influences including corner effects and, since it is not linearized, accurate fluid properties for variations in state. In the 'Multiphysics' model, the sinusoidal velocity driver has a peak amplitude of 1E-5 m/s, which is well within the acoustic regime as discussed later. The 'Multiphysics' model, while more computationally intensive, has a major advantage in that it can serve as a point of departure so more complex influences can be studied and understood, such as high-amplitude waves, considerations for liquids, and flow effects.

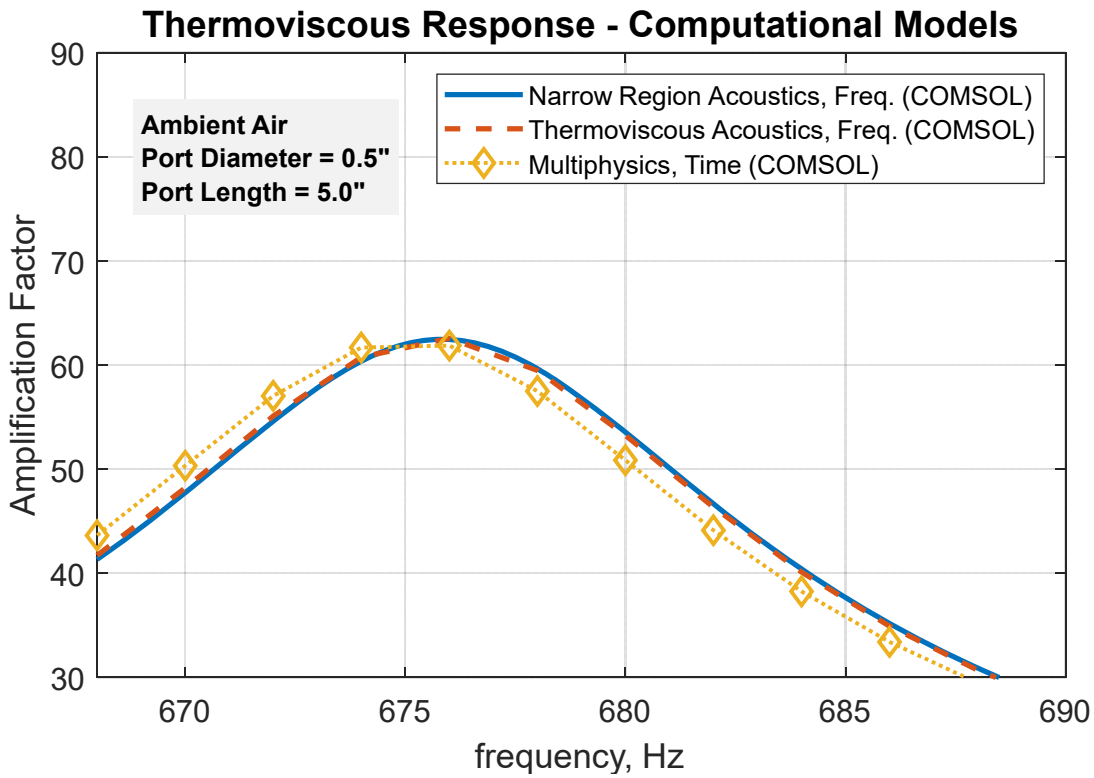

Figure 15. Thermoviscous Response for a Sensor Port – Computational Models, Detailed View

The absorption coefficient of a simple cylindrical port can also be extracted using COMSOL simply by using eq. (26) and eq. (14) to obtain eq. (76), where $\hat{p}$ is the complex total acoustic pressure and the subscripts refer to the locations.

$$\alpha_{port} = \Re\left[\frac{1}{L}\operatorname{arcsech}\left(\frac{\hat{p}_{back}}{\hat{p}_{inlet}}\right)\right] \tag{76}$$

Figure 16 shows a comparison of the absorption coefficients using several COMSOL and analytical models over a wide bandwidth and a detailed view near the resonant frequency. Note that for numerical models, the absorption coefficient is the overall effective absorption coefficient for the model obtained using eq. (13) and eq. (14), and not the same as the analytic absorption coefficient, e.g., such as eq. (39). There could be additional effects that are not necessarily captured in the analytic models. The 'Narrow Region Acoustics' model compares identically with the 'Exact' model as expected, however there is a clear difference between these and the 'Traditional' model. There is also a small difference observed in the more accurate 'Thermoviscous' computational model.

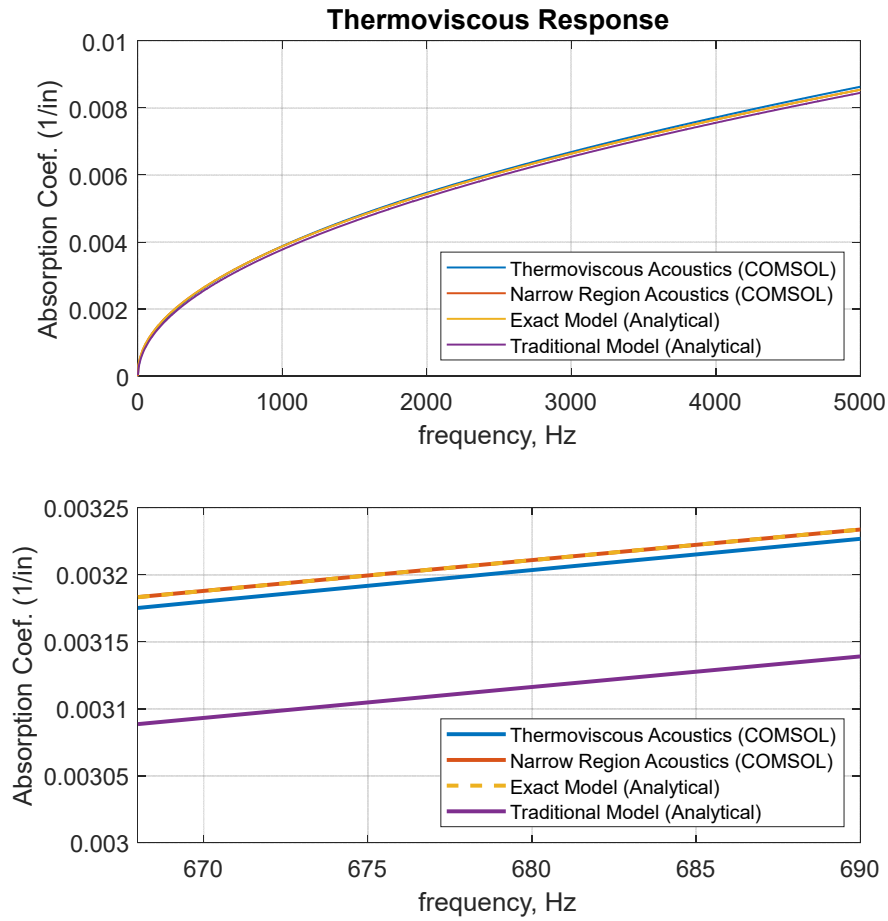

Figure 16. Absorption Coefficient Comparison: Full Bandwidth (top) and Zoomed-in View (bottom)

As a final thermoviscous analysis, the viscous and thermal boundary layers are plotted at the port midpoint location (at 2.5 in). Figure 17 shows a zoomed-in view of the boundary layers near the port wall (at 0.25 in) showing acoustic velocity and temperature perturbations. The boundary layers are plotted every 1.18E-4 seconds for 13 time steps, which is just over a full cycle at 676 Hz (the fundamental frequency). A similar plot showing the viscous boundary layer is described in reference [**3** p. 230]. The oscillatory boundary layers are produced due to the frictional shear force that is exerted on the fluid and the heat transfer that takes place between the fluid and surface.[2 p. 322] Viscous and thermal losses are present when there are gradients in the velocity field and temperature, respectively, as described by the viscous shear diffusive loss terms in the momentum equation and thermal conduction diffusive loss term in the energy equation.[15] The transition to the no-slip and isothermal conditions at the wall therefore produces the acoustic boundary layers as the fluctuations move through the port.[15]

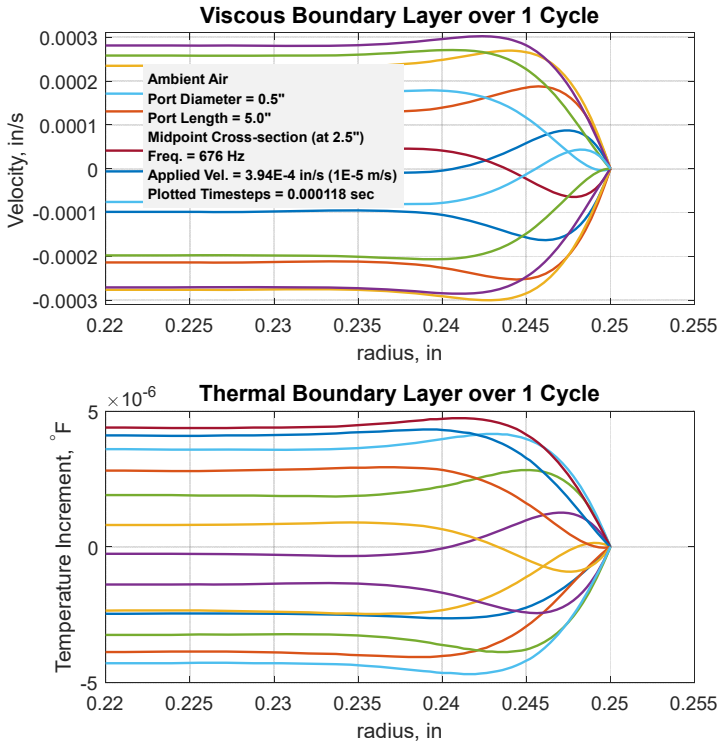

Figure 17. Viscous and Thermal Boundary Layer

Modeling Thermoviscous Effects of Nonlinear Amplitudes

The previous example configuration was focused on the thermoviscous response from an acoustic wave. In this section, nonlinear or finite-amplitude waves are studied, however the same example configuration is examined. For an unsteady oscillation, the small-signal approximation is satisfied with the following restrictions on acoustic pressure and particle velocity given in eq. (77) or eq. (78).[2] p. 36

$$|p| \ll \bar{\rho}\bar{c}^2 \tag{77}$$

$$|u| \ll \bar{c} \tag{78}$$

For air at the conditions in this example, the acoustic pressure and particle velocity amplitude must be *much less than* 20.6 psi (142,032 Pa) or 1135 ft/s (346 m/s) to satisfy the small-signal approximation. These values seem large, however considering that the 'much less than' inequality implies several orders of magnitude, an acoustic oscillation in air can be approximated roughly with less than two orders of magnitude or at no more than 0.2 psi and 11.4 ft/s (3.5 m/s). In this example, the response for three cases are compared. In the three cases, the sinusoidal velocity driver has a peak amplitude of 3.94E-4 in/s (1E-5 m/s), 196.85 in/s (5 m/s), and 393.70 in/s (10 m/s). The maximum peak pressure in these cases reaches a value of 5.95E-7 psi (4.1E-3 Pa), 0.331 psi (2279 Pa), and 0.851 psi (5866 Pa), respectively at 676 Hz. It is observed that the highest-amplitude case maintains a clear waveform distortion, and the minimum pressure of the waveform only achieves a magnitude of 0.613 psi (4229 Pa).

For nonlinear problems, numerical convergence can be more difficult. Additional solver characteristics may need to be considered. The default damped Newton's method solver uses a constant damping parameter method (where the baseline approach has no damping) and is adequate to prevent

convergence errors for the acoustics models. However, for nonlinear waves, this method may often be unsuccessful. One alternative is to use the automatic damped Newton's method solver. This solver automatically determines a needed damping factor for every iteration to aid in resolving a root. In the examples studied, this increases the solution time substantially to over 20x longer than the 'Multiphysics' acoustics model described previously, but is often the only necessary step in resolving the solution. This method was used in providing solutions to nonlinear problems and verified by comparing results for the acoustics model. Additionally, it may take longer to reach stationarity in the nonlinear problems where the peak amplitudes no longer change. In the current examples, this usually required approximately a duration of 100 periods, but at times required up to 400 periods.

Because nonlinearities may include harmonics and other nonlinear modulations through the complete spectrum, additional considerations must be made for the time-stepping solver and mesh. A sensitivity showed that the solver time steps should be at least 60x smaller than a single period for accurate amplitude resolution. This is also the recommended resolution by COMSOL. Depending on the amplitude level within the domain, a number of harmonics may be desired for an accurate representation of the nonlinear waveform. For the nonlinear example here, the fundamental and 9 additional harmonics are desired. Ten total harmonic modes is adequate for an overall amplitude comparison as there is a progressive reduction in amplitude for higher harmonics. The example configuration discussed previously resulted in a peak amplitude at 676 Hz for air. In the 676 Hz case with the additional harmonics, the highest frequency of interest is 6760 Hz. With the highest frequency of interest equal to 10x the fundamental and considering the Nyquist frequency for data processing, a minimum output sampling rate of 20x smaller than the fundamental period is required. In addition, to accurately represent the amplitude at 10x the fundamental frequency, a time step of 60x smaller than the period of the highest frequency (6760 Hz) is needed as noted earlier, which equates to a computational time step that is 600x smaller than the fundamental period (676 Hz). This ensures the amplitude at the highest frequency can be resolved accurately. While the output sampling rate is given as a minimum needed for data processing to best manage file size, the computational time step must be much more resolved. This analysis is a prudent step; however, a sensitivity should always be done to ensure amplitude resolution.

To accurately account for this full bandwidth, the boundary layer thickness should be calculated at the maximum desired frequency, which is 6760 Hz in the example. This ensures the smallest boundary layer is captured**.** Since the first layer is based on the boundary layer thickness, i.e., 0.2x the minimum thickness in the example, the first layer will be smaller at the higher frequency. The most important boundary layer feature is that there are enough elements to capture details from the smallest boundary layer. The overall mesh of this example includes 10470 elements and 7270 mesh vertices with tri elements in the interior and quad elements for the boundary layer.

A comparison showing the acoustic response and the two other finite-amplitude responses are shown in Figure 18. This shows a clear damping effect with increased oscillation amplitude. Additionally, a peculiar response is evident in the response of the largest oscillation amplitude near 680 Hz and 684 Hz. Additional simulations were performed to help resolve the characteristics of the response near this bandwidth. This secondary resonance, which actually exceeds the primary resonance in amplification for the 10 m/s case, is also noticeable in the 5 m/s response case as a slight bulging in the same frequency range. It is not clear as to the cause of this nonlinear effect, although there are several additional factors that could play a role such as transverse flow near corners, finite-amplitude wave propagation speed and characteristics, or separate propagation regimes within the central region and near the boundary region**.**[19] pp. 44-47, [20] pp. 285-297

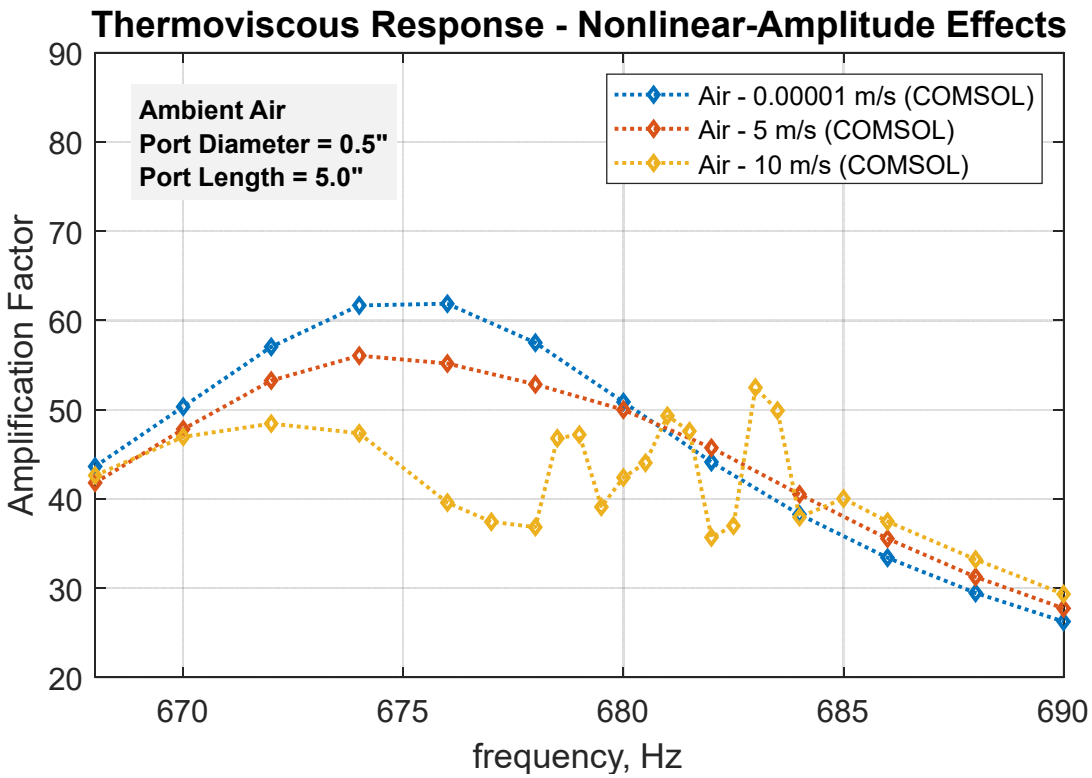

Figure 18. Thermoviscous Response – Nonlinear-Amplitude Effects

Sensor Port Model

To model the acoustics in a sensor port, two very important physical mechanisms are considered. The radiation acoustics at the port opening and the thermoviscous dissipation along the walls of the port. In this section, a simple sensor port is modeled numerically in COMSOL and analytically using the framework described in this paper.

The sensor port model can be studied numerically using the COMSOL *Pressure Acoustics, Frequency Domain* interface. As noted previously, this interface is suited to model pressure variations for the propagation of acoustic waves in fluids at quiescent background conditions.[15] For the thermoviscous effects, the COMSOL *Narrow Region Acoustics* node is used rather than using the COMSOL *Thermoviscous Acoustics* interface. The error in using this thermoviscous model was shown previously to be very small and saves a large computational expense.

For comparisons to the numerical solution, the wave equation is solved analytically using an appropriate propagation constant for the thermoviscous dissipation and for the radiation acoustics. The 2-line model, eq. (34), is used so that both the propagation constant in the port, eq. (51), and in the radiation acoustics region, eq. (72), can be incorporated. The characteristic impedance used in the model is given simply as eq. (20). The thermoviscous effects are modeled over the length of the port and the radiation effects are modeled over the length of the end correction. Combining both effects in this manner results in a very accurate acoustic port response solution.

Example Sensor Port

An example using the COMSOL pressure acoustics model is described first and then compared to the analytical solution. The response associated with a port of radius 0.25 in (0.00635 m) and length of 1 in (0.0254 m) is studied in ambient air. The shorter length compared to previous examples is used to emphasize the effects of acoustic radiation. The air is at a temperature of 77 °F (298.15 K) with sound

speed 1136 ft/s (346 m/s) and density 4.2779E-5 lb_m/in^3 (1.1841 kg/m^3). For an equal comparison of the sensor port model computational and analytical models, these and other properties are specified and listed in Table 2. While the resolution of the tabulated values seems excessive, small differences can produce minor but observable differences. The domain and mesh configuration is based on the previously verified piston function and thermoviscous models.

Table 2. Properties for Sensor Port Example

Property	Units	Value
Dynamic Viscosity	Pa·s	1.838544078E-05
Specific Heat Ratio	-	1.399375426
Heat Capacity at Constant Pressure	J/(kg·K)	1005.630524639
Density	kg/m3	1.184121471
Thermoal Conductivity	W/(m·K)	0.026162083
Speed of Sound	m/s	346.040793864

Similar to the flanged circular piston example described previously, the total domain radius is 7.5 in (0.1905 m), which is 30x the port radius, and includes a 0.375 in (0.009525 m) thick PML that behaves as an absorptive boundary. A grid refinement region is also defined at 10x the port radius near the far field transition radius. The analysis is explored over the bandwidth through 10,000 Hz by increments of 1 Hz. The minimum wavelength of interest is therefore 1.3632 in (at 10,000 Hz).

Domain Setup

Figure 19 shows the baseline domain setup for modeling a sensor port. As noted previously, an advantage of numerical analysis is that a direct comparison can easily be made by comparing solutions of the exact configuration with a sensor port and the desired configuration with no sensor port. A secondary domain consists of the exact same configuration except no sensor port. To automate this using COMSOL, a *Parametric Sweep* node can be added to the COMSOL *Study*.

In the parametric sweep, the response is calculated without the port first and then subsequently with the port. This is performed in COMSOL within the *Parametric Sweep* node by varying the value of the port length parameter where the baseline length could be specified in the *Parameters* node.

The domain setup is very similar to the previous configuration shown in Figure 8. There is the additional port region where the *Narrow Region Acoustics* node is applied. In addition, another arc is defined at a radius equal to $R \cdot \sqrt{\frac{64}{9\pi^2}+1}$ based on eq. (2) that encompasses the end correction region entirely.

Finally, the port is simulated to be in the presence of a background acoustic field. To eliminate any directional dependence, a diffuse field can be created in the simulation. Note that COMSOL uses the scattered field formulation where the total acoustic pressure is the sum of the background acoustic pressure and the scattered acoustic pressure.[21] pp. 52-53, 75-76, 200-204 This formulation is convenient to study the effect of incident pressure waves and scattering problems. For the sensor port analysis the *Background Pressure Field* node can be used to set an existing diffuse field by selecting a plane wave pressure field with a 0 unit vector. This simplifies the field such that it is spatially independent with a uniform sound pressure everywhere in the domain. For this linear analysis, the background acoustic pressure amplitude is set simply to 1 Pa. The total acoustic pressure field is the relevant acoustic variable for analysis, which is representative of a direct acoustic measurement in a sensor port configuration.

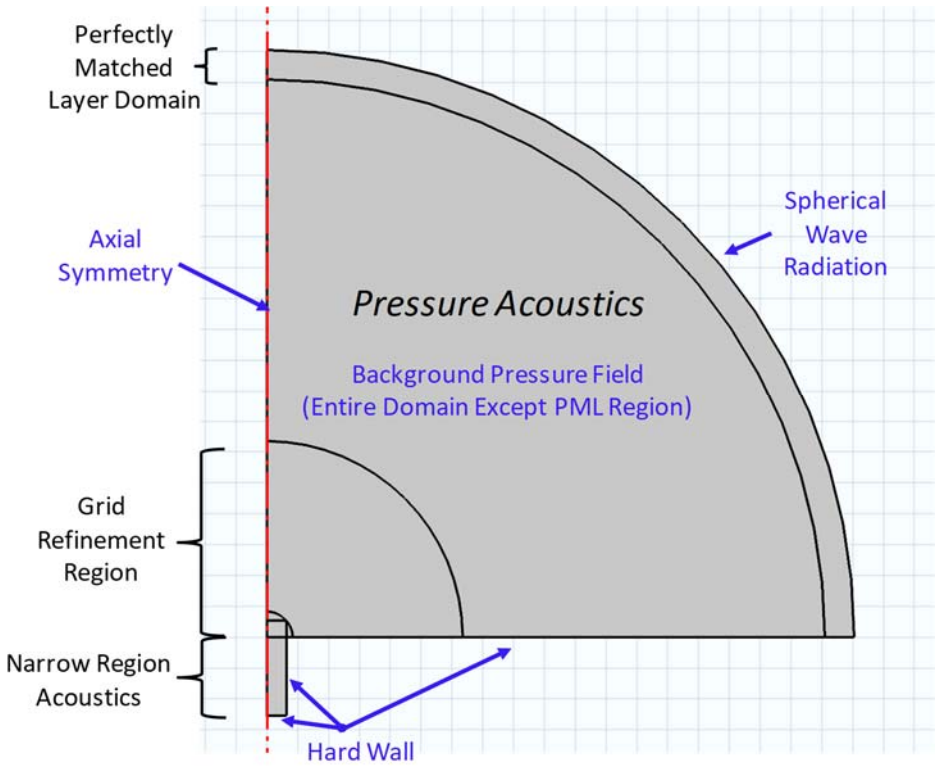

Figure 19. Modeling Senor Port Response - 2-D Axisymmetric Baseline Domain Setup

Mesh Design

To ensure the physics were captured accurately, the model was first broken down into radiation acoustics and thermoviscous acoustics as described in previous sections. The mesh considerations discussed in these sections were applied here to ensure that these physics are captured accurately in the sensor port model. For simplicity, the mesh in the grid refinement region is extended into the port where the *Narrow Region Acoustics* node is applied.

Comparison of Numerical and Analytical Solution

In this section, the pressure transfer function is examined in the sensor port model and compared between the numerical and analytical solution. In general, the pressure amplification factor and relative phase are obtained from eq. (10) and eq. (11). Since the COMSOL simulation separately computes the complex pressure distribution for a case with the sensor port and a case without the sensor port, careful considerations of the computations must be made. Computing the pressure amplification factor using the complex pressure from two separate simulations is straight forward using eq. (10). However, since the phase angle is not a measurement within a single simulation domain, a general form must be used to evaluate the relative phase angle between two complex numbers. Equation (79) can be used to calculate the phase angle in the range $-\pi < \phi \leq \pi$, for complex vectors $\bar{a} = a_r + a_i i$ and $\vec{b} = b_r + b_i i$.

$$\phi = \tan 2^{-1}\left(a_r b_i - a_i b_r,\ a_r b_r + a_i b_i\right) \tag{79}$$

Figure 20 shows the comparison of the analytical model and numerical model. As noted earlier, eq. (20), eq. (34), eq. (51), and eq. (72), are used to plot the analytical solution while the numerical solution is obtained directly from COMSOL.

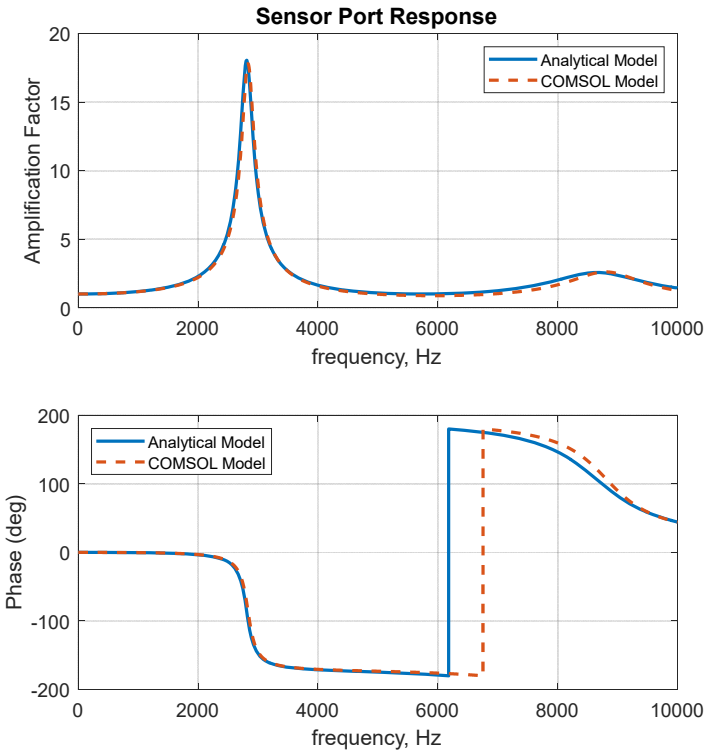

Figure 20. Sensor Port Response Analytical and Numerical Comparison

The results show a very good comparison and encompass the dissipation associated with both thermoviscous effects and radiation acoustics. A separate COMSOL simulation was also run considering just the thermoviscous effects in the port. This does not include the radiation acoustics and a comparison to this solution would show the effect of attenuation associated with radiation acoustics. The resulting pressure amplification curve is not shown, however the peak amplification is found as 142.3x at 3391 Hz for the example port configuration. This can also be estimated using eq. (26) and eq. (51).[8] The dramatic reduction in amplification due to radiation acoustics to a peak amplification of 17.8x at 2834 Hz is observed in Figure 20. This emphasizes the importance of including radiation acoustics in a sensor port frequency response model.

Figure 21 shows a zoomed-in view of the fundamental quarter-wave response. The small discrepancy observed between the analytical solution and numerical simulation is due to assumptions in the analytical model. Most likely, the largest error results from modeling radiation acoustics using the piston model, which assumes a uniformly distributed flow field at the port opening. The reality is that there is a complex flow field near the port opening, however a uniform flow field is a good approximation.

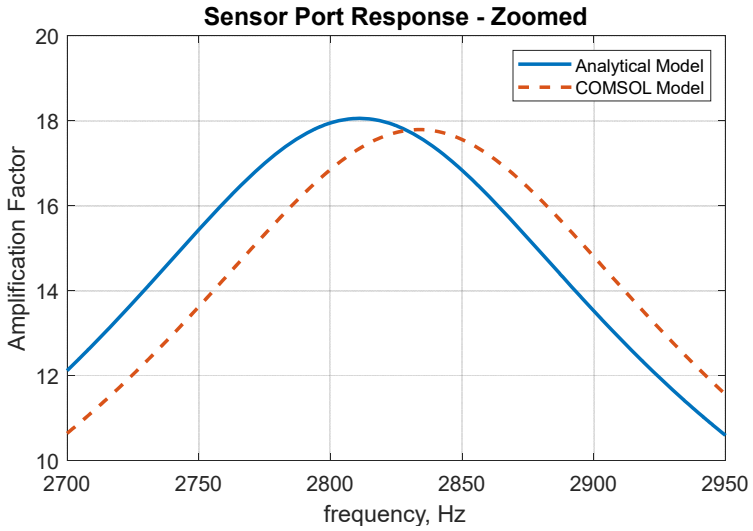

Figure 21. Sensor Port Response Analytical and Numerical Comparison - Zoomed

Figure 22 shows a zoomed-in snapshot of the velocity vector field at the opening where the flange intersects the port. The snapshot is for the resonance condition at 2834 Hz and it is clear that the instantaneous velocity field is not uniform across the entire opening. Recall that this particular simulation uses the *Narrow Region Acoustics* node where the dissipation is distributed evenly within the fluid, so boundary layers will not be evident in the velocity field. The boundary layer will further complicate the flow field at the opening.

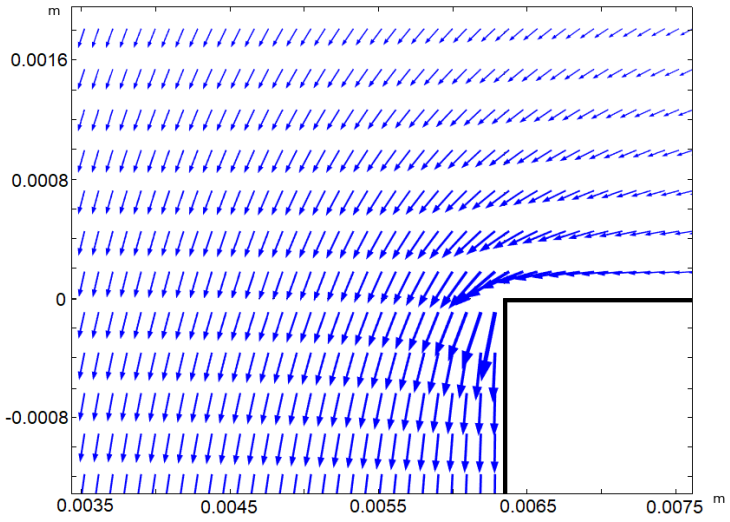

Figure 22. Velocity Field at the Opening (Snapshot at Resonance) - Zoomed

Figure 23 shows a contour plot of the total pressure field in and around the sensor port at the fundamental quarter-wave resonance (2834 Hz) and the three-quarter-wave resonance (8799 Hz). The pressure node lines for the quarter-wave mode are dark red and for the three-quarter-wave mode are light green. To discern the node line color, a simple gage is to view the color in the plenum far from the port where the pressure response is effectively zero. The plots show the effect of the port opening on the spatial pressure field.

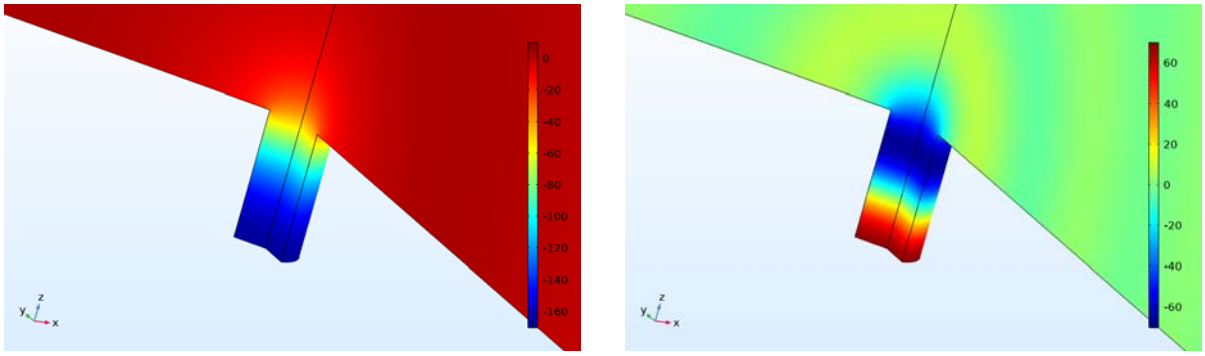

Figure 23. Total Pressure Contour Plot: Quarter-Wave Mode at 2834 Hz (left) and Three-Quarter-Wave Mode at 8799 Hz (right)

SPECIALIZED FILTER DESIGN

A specialized filter is designed such that it can be applied to data and modify the data based on the sensor port transfer function. In most cases, a filter is used to pass certain frequencies and reject others, but in general a filter is a device that modifies certain frequencies relative to others.[22 p. 439] The transfer function shown in Figure 20 can be modified and converted into a filter, and subsequently applied to the data. For example, simulated data can be generated and the transfer function can be directly applied to the data to understand the effects of the port response. Alternatively, the inverse transfer function can be estimated and then applied to data to remove the sensor port effects. Note that the *analytical* sensor port response from Figure 20 is used in this analysis, which has a peak resonance at 2811 Hz and amplification factor of 18.1x.

The procedure to apply a filter based on the frequency response function is relatively straightforward. The software tool PC-SIGNAL® [23] by AI Signal Research, Inc. has the procedure entirely automated and is used to perform the analysis in this section. This software tool is a specialized dynamic signature analysis software package for rocket engine and rotating machinery health monitoring, fault detection, and diagnostics. It incorporates the conventional signal analysis capabilities as well as state-of-the-art signature analysis technologies that have been developed over years of research on dynamic data, particularly from the Space Shuttle Maine Engine.

Conceptually, the procedure is very simple. The impulse response describing the transfer function must first be obtained. This is done by computing the inverse discrete Fourier transform of the transfer function. Then, by convolving the impulse response with the data signal, a modified time history is obtained. The convolution step allows the impulse response to be used effectively as a 'filter' where the filter characteristics are described by the features of the transfer function, i.e., the filter provides gain and phase characteristics as defined by the transfer function.

Verification can be performed that shows the specialized filter is free of signal artifacts associated with Gibbs phenomena by computing the frequency response function of the impulse response function while zero-padding. However, in general, the transfer function gain is relatively smooth compared to typical steep roll-off bandpass and band-stop filters. Typically the concern occurs with wrapped phase angles where a sudden jump in phase occurs, however if necessary the phase can be smoothed with minimal effect on the signal.

To correct data that is known to be contaminated by a sensor port response, the inverse transfer function has to be estimated. The inverse transfer function, eq. (80) and eq. (81) are analogous to the sensor port response given previously as eq. (10) and eq. (11). For lack of nomenclature, the amplification factor and relative phase of the inverse transfer function will be referred to as the inverse sensor port response.

$$\widehat{X}(f) = \left| \frac{\hat{p}_D}{\hat{p}_U} \right| \tag{80}$$

$$\widehat{\phi}(f) = \angle \left(\frac{\hat{p}_D}{\hat{p}_U} \right) \tag{81}$$

Using the example that produced Figure 20 (the analytical model solution), the inverse sensor port response is shown in Figure 24.

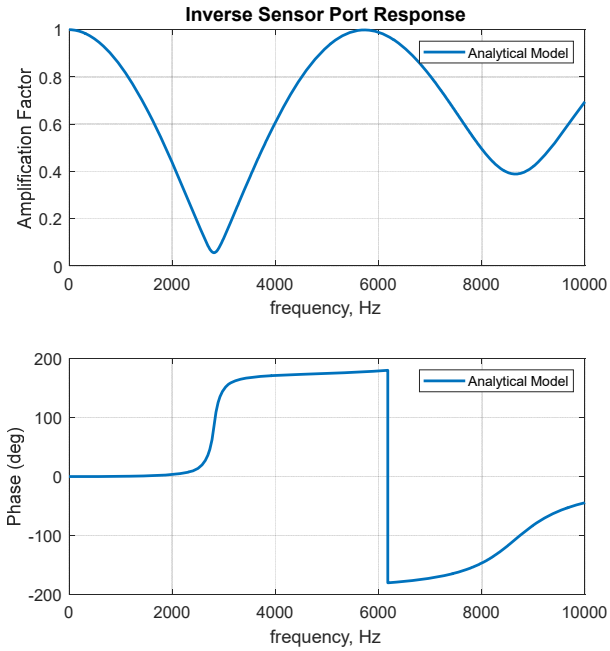

Figure 24. Inverse Sensor Port Response

The transfer function described in Figure 24 is truncated at 10 kHz since this domain was determined to be the relevant data range for the example, however an analytic model can be estimated over any frequency bandwidth. From 10 kHz to the Nyquist frequency of the simulated data (50 kHz), the amplification factor and phase are set at zero. In general, truncation in this fashion may not be an ideal approach in filter design as sudden changes can introduce Gibbs phenomena, and a smooth roll-off may be better suited, however this was a simple modification and done for the example. To use the advantage of processes suited for power of 2, the number of points that make up the transfer function is set to 16,385 points which gives the transfer function a frequency resolution of 3.0518 Hz. The impulse response of the transfer function is obtained by estimating the inverse discrete Fourier transform and subsequently applying a half block time delay to the result using a circular shift. This introduces a known time delay that is later corrected, but most importantly, it centers the impulse response function to help minimize discontinuities. The filter order of the impulse response is 32,768 points and a zoomed in section near the center is shown in Figure 25. The impulse response function contains all the information necessary to describe the transfer function and can be used as a specialized filter.

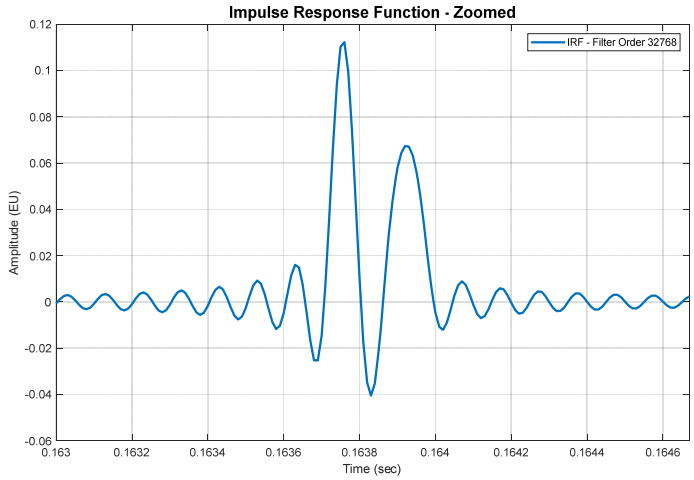

Figure 25. Impulse Response Function for Example

To investigate the effect of the specialized filter on real data, two sets of simulated data are first generated at 100,000 sps shown in Figure 26. A 10-second time series is generated that contains uniformly distributed random numbers in the open interval from -1 to 1. Another 10-second time series is generated that is simply a sinusoid at 2811 Hz; this frequency occurs at the resonance of the sensor port response (the analytical model solution) or antiresonance of the inverse sensor report response shown in Figure 24.

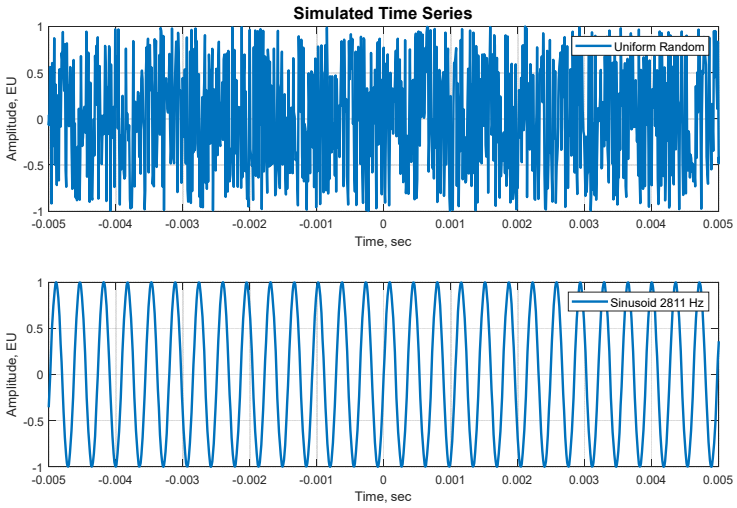

Figure 26. Simulated Time Series – Uniform Random (top) and 2811 Hz Sinusoid (bottom)

As noted earlier, the impulse response is subsequently convolved with the original simulated data to produce the filtered data time series. Figure 27 shows a power spectral density (PSD) overlay plot of the original uniform random data and the newly filtered data. The original uniform random data is constant over all frequencies for a PSD, which makes it a useful data set for examining filter effects.

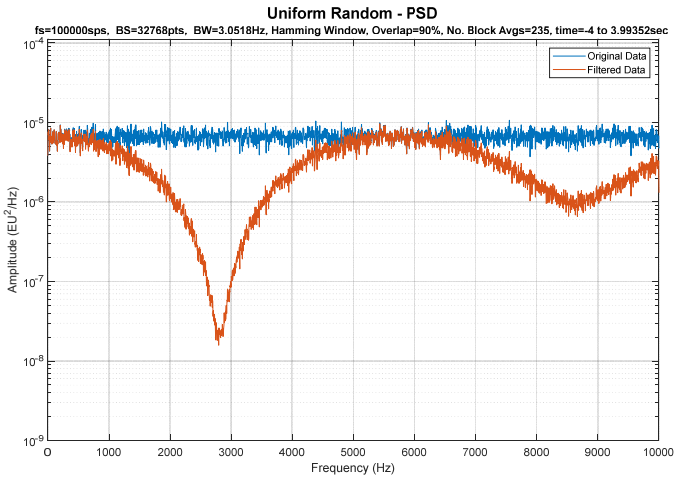

Figure 27. Power Spectral Density Plot – Original Uniform Random Data and Filtered Data

A transfer function estimate can be made by computing the ratio of the cross power spectral density and reference power spectral density.[24] pp. 78-81, 105 The two signals for the estimated transfer function are the original simulated uniform random data and the filtered uniform random data, i.e., filtered using the specialized filter. A data block size of 32,768 points is selected to process the transfer function since it will result in the same frequency resolution of 3.0518 Hz for the 100,000 sps data. This data block size is not necessary, but will produce a point-to-point comparison to the initial transfer function filter. A comparison of the initial transfer function filter to the estimated transfer function using the uniform random data is shown in Figure 28. In fact, the comparison is so close, that the frequency axis is shown through 11 kHz to show the computed transfer function estimate actually uses the data. The transfer function estimate attempts to produce zero values for the amplitude at frequencies higher than 10 kHz to match the initial truncated transfer function specification. This results in an extremely small amplitude close to zero and a random phase.

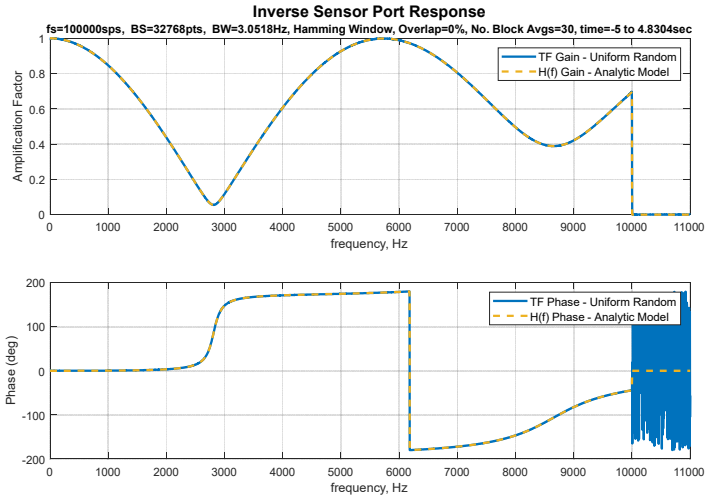

Figure 28. Transfer Function Comparison using Uniform Random Data

Finally, the same filter is applied to the simulated sinusoidal data. The original data and the filtered data are overlaid and zoomed in Figure 29 to show the amplitude reduction of 18.1x and the phase shift of +86˚ recalling that a positive phase shift shifts a sinusoid in the negative direction. The amplification reduction and relative phase compares exactly to the values selected at the resonance

frequency (2811 Hz) directly from the inverse transfer function in Figure 24. This indicates that the filtered data were appropriately modified based on the inverse transfer function.

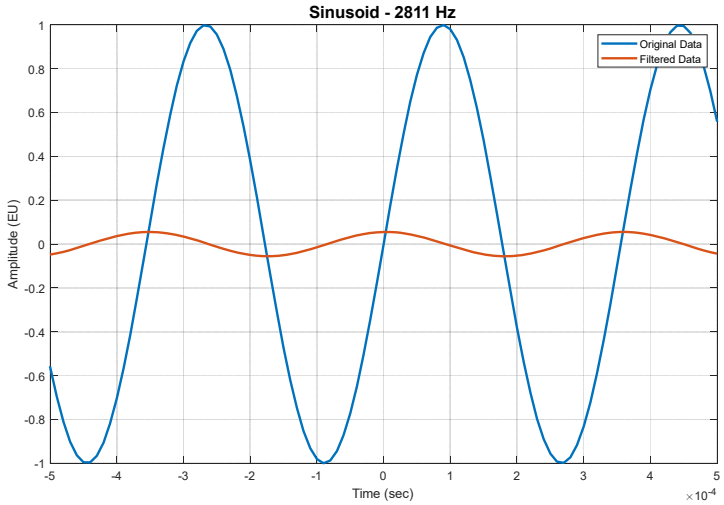

Figure 29. Sinusoidal Comparison

This filtering procedure is very powerful and can be used to predict the effect of a sensor port on data or to make corrections to data that is influenced by sensor ports.

SUMMARY AND CONCLUSIONS

A sensor port is part of the system being measured, but it is not part of the system that is intended to be measured. Even a short sensor port may have an adverse contribution to collected data. Surprisingly, limited analysis has been described on the determination of the overall frequency response of a recessed acoustic cavity, where models in the literature using lumped acoustic elements fall short due to their extreme assumptions.[3 p. 283] The acoustic resonance within the sensor port produces a frequency-dependent amplification and phase deviation that directly affects the data collected.

Traditional design criteria for recess length are based on an undamped forced oscillator frequency response model. This model is improved in this paper to directly incorporate an end user's acceptable error. While this model provides a guide for a sensor port design, it does not produce a representative frequency response, and breaks down in many cases such as at frequencies closer to the resonance or in multi-port designs. Estimates that are more accurate may even allow the recess to be lengthened, for example, so a more accurate estimate may be desired. Additionally, an accurate estimate could be useful for correcting data.

As an advancement to the undamped SDOF model used classically for sensor port analysis, a theory is developed for obtaining the actual acoustic frequency response of a sensor port. Three critical advancements were necessary to extend the classic acoustic theory into a practical sensor port frequency response model. The application of a distributed acoustic model rather than the classic lumped acoustic elements were necessary to capture the higher frequency effects. The development of a practical form of the exact solution to the thermoviscous wave equation was necessary for use in the propagation constant model. The reformulation of acoustic radiation impedance as an acoustic propagation constant was also necessary for use in the propagation constant model. Two dissipation mechanisms are required for an accurate sensor port analysis, i.e., thermoviscous effects and radiation acoustics. The distributed acoustic model framework can incorporate these effects for a constant diameter sensor port by applying a 2-line model. An analytic form is derived for the 2-line model so that the response can be predicted quickly, easily, and accurately. Pseudocode is also presented for a multiline model so the frequency response of more complex sensor ports can be modeled.

A primary advantage of a computer simulation, or numerical modeling, is to tackle problems that are too complex for analytical solutions. A major advantage, aside from the ability to model sophisticated physical problems and a 3-dimensional geometry, is that the models are deterministic. This is an advantage since a direct comparison can easily be made by numerically comparing the solutions of the exact configuration (with a sensor port) and the desired configuration (usually with no sensor port). Simulating the exact configuration and the desired configuration separately using all of the identical simulation conditions, e.g., same excitation source and same boundary conditions, allows pertinent quantities of interest between the two configurations to be obtained very precisely and compared. Using this procedure an accurate transfer function can be obtained for any sensor port system. The theory for this comparative analysis is developed and described throughout. The innovative yet very basic procedure is remarkably powerful when combining solutions from deterministic numerical simulations.

As part of the verification procedure for the sensor port simulation, piston functions and thermoviscous responses are modeled separately. Comparing to known analytical results allows confidence in the sensor port domain and mesh design since the sensor port response encompasses the same dissipation processes. Piston functions, which are the basis for the radiation acoustics model, are simulated numerically and compared to analytic models with exact reproduction. The effective length, or end correction of a port, is studied numerically as well showing that there is a significant frequency dependence.

Thermoviscous effects are simulated and compared to analytic models, also with exact reproduction. Simulations using more sophisticated thermoviscous models are also performed, including applying the linearized Navier-Stokes or more advanced multiphysics simulations. These models are executed to help understand physics associated with deviations from the simpler models. The thermoviscous responses associated with nonlinear-amplitudes are described showing a clear damping effect with increased oscillation amplitude, however also producing secondary resonances.

A sensor port is modeled numerically and compared to the newly developed analytic theory. The results show a very good comparison and encompass the dissipation associated with both thermoviscous effects and radiation acoustics. The transfer function – eq. (10) and eq. (11), characteristic impedance – eq. (20), transfer equation – eq. (34), and propagation constants – eq. (51), and eq. (72), can be used to plot the analytical solution of a constant diameter sensor port response. The pseudocode described in the text can be used for more complex systems.

A specialized filter is designed such that it can be applied to data and modify the data based on the sensor port transfer function. The filter is applied to simulated data to show the influence on data. This filter procedure is very powerful and can be used to predict the effect of a sensor port on data or to make corrections to data that is influenced by sensor ports.

ACKNOWLEDGEMENTS

Note that a separate NASA Technical Publication includes further details and is being finalized for publication. I would like to acknowledge my mentors Tom Nesman and Tom Zoladz for encouraging me to study this problem and provide very useful insight. My colleague, Sean Fischbach, was also very helpful in reviewing the ideas and providing important insight. Jess Jones, Thein Shi, and Jen-Yi Jong from AI Signal Research, Inc have been very helpful in understanding the signal processing aspects in this paper.

REFERENCES

1. Blevins, R. D. *Formulas for Natural Frequency and Mode Shape*. Malabar, FL, Krieger Publishing Company, 2001.
2. Blackstock, D. T. *Fundamentals of Physical Acoustics*. New York, John Wiley & Sons, Inc., 2000.
3. Kinsler, L. E., Frey, A. R., Coppens, A. B., and Sanders, J. V. *Fundamentals of Acoustics*. New York, John Wiley & Sons, Inc., 2000.
4. Harrje, D. T., and Reardon, F. H. "Liquid Propellant Rocket Combustion Instability." NASA SP-194, Washington, DC, 1972.

5. Thomas, J. P., and Layton, J. P., "Final Summary Technical Report on Transient Pressure Measuring Methods Research," Princeton University: Guggenheim Laboratories for the Aerospace Propulsion Sciences, 31 Mar. 1967.
6. Wylie, E. B., and Streeter, V. L. *Fluid Transients in Systems*. Upper Saddle River, NJ, Prentice-Hall, Inc., 1993.
7. Tijdeman, H. "On the Propagation of Sound Waves in Cylindrical Tubes," *Journal of Sound and Vibration* Vol. 39, No. 1, 1975, pp. 1-33.
8. Casiano, M. J., and Zoladz, T. F. "Theoretical Consolidation of Acoustic Dissipation." NASA/TM-2012-217455, 2012.
9. Munjal, M. L. *Acoustics of Ducts and Mufflers*. New York, John Wiley & Sons, 1987.
10. Morse, P. M., and Ingard, K. U. *Theoretical Acoustics*. New York, NY, McGraw-Hill, Inc., 1968.
11. Kinsler, L. E., and Frey, A. R. *Fundamentals of Acoustics*. New York, John Wiley & Sons, Inc., 1962.
12. Aarts, R. M., and Janssen, A. J. E. M. "Approximation of the Struve Function H_1 occuring in Impedance Calculations," *The Journal of the Acoustical Society of America,* Vol. 113, No. 5, 2003, pp. 2635-2637.
13. Aarts, R. M., and Janssen, A. J. E. M. "Efficient Approximation of the Struve Function H_n occuring in the Calculation of Sound Radiation Quantities," *The Journal of the Acoustical Society of America,* Vol. 140, No. 6, 2016, pp. 4154-4160.
14. "COMSOL Multiphysics Version 5.4." COMSOL Inc., 1998-2018.
15. "COMSOL Multiphysics Reference Manual, version 5.4." COMSOL, Inc., www.comsol.com.
16. Pierce, A. D. *Acoustics, An Introduction to its Physical Principles and Applications*. New York, McGraw-Hill Book Company, 1981.
17. Foote, K. G. "Discriminating Between the Nearfield and Farfield of Acoustic Transducers," *The Journal of the Acoustical Society of America,* Vol. 136, No. 4, 2014, pp. 1511-1517.
18. Bird, R. B., Stewart, W. E., and Lightfoot, E. N. *Transport Phenomena, Revised Second Edition*. New York, John Wiley & Sons, Inc., 2007.
19. Hamilton, M. F., and Blackstock, D. T., eds. *Nonlinear Acoustics*. San Diego, CA, Academic Press, 1998.
20. Anderson, J. D. *Modern Compressible Flow with Historical Perspective*. Boston, McGraw-Hill, 2003.
21. "COMSOL Multiphysics Acoustics Module User's Guide, version 5.4." COMSOL, Inc., www.comsol.com.
22. Oppenheim, A. V., and Schafer, R. W. *Discrete-Time Signal Processing*. Upper Saddle River, NJ, Prentice-Hall, Inc., 1999.
23. "PC-SIGNAL® ". AI Signal Research, Inc., 1993-2019.
24. Bendat, J. S., and Piersol, A. G. *Engineering Applications of Correlation and Spectral Analysis*. New York, John Wiley & Sons, Inc., 1993.